Recent Advance in Understanding the Dynamics of the Madden-Julian Oscillation

Tim LI[1,2*] (李天明)

1 *International Pacific Research Center and Department of Meteorology, School of Ocean and Earth Science and Technology, University of Hawaii at Manoa, Honolulu, Hawaii* 96822, *USA*

2 *Key Laboratory of Meteorological Disaster and College of Atmospheric Science, Nanjing University of Information Science & Technology, Nanjing* 210044, *China*

(Received December 14, 2013; in final form January 6, 2014)

ABSTRACT

The Madden-Julian oscillation (MJO) is a dominant atmospheric low-frequency mode in the tropics. In this review article, recent progress in understanding the MJO dynamics is described. Firstly, the fundamental physical processes responsible for MJO eastward phase propagation are discussed. Next, a recent modeling result to address why MJO prefers a planetary zonal scale is presented. The effect of the seasonal mean state on distinctive propagation characteristics between northern winter and summer is discussed in a theoretical framework. Then, the observed precursor signals and the physical mechanism of MJO initiation in the western equatorial Indian Ocean are further discussed. Finally, scale interactions between MJO and higher-frequency eddies are delineated.

Key words: Madden-Julian oscillation (MJO), eastward phase propagation, physical mechanism of MJO initiation, scale interaction

Citation: Li, Tim, 2014: Recent advance in understanding the dynamics of the Madden-Julian oscillation. *J. Meteor. Res.*, **28**(1), 001–033, doi: 10.1007/s13351-014-3087-6.

1. Introduction

The Madden-Julian oscillation (MJO; aka Intraseasonal Oscillation (ISO)) is the most prominent mode of intraseasonal variability in the tropics[1]. First identified by Madden and Julian (1971) using single station data from Canton Island, MJO is characterized by a zonal wavenumber one structure with a thermal direct vertical cell propagating eastward along the equator (Madden and Julian, 1972). Later analyses with satellite, reanalysis, field campaign (such as Asian Monsoon Experiment, MONEX), and model data confirmed the planetary zonal scale of MJO and showed that the oscillation is more broadband than the original 40–50-day period identified by Madden and Julian (1971) and can span a range of 10–90 days (Krishnamurti and Subrahmanyam, 1982; Weickmann, 1983; Krishnamurti, 1985; Murakami and Nakazawa, 1985; Weickmann et al., 1985; Lau and Chan, 1986; Knutson and Weickmann, 1987; Chen and Murakami, 1988; Chen et al., 1988; Hartmann and Michelsen, 1989; Sperber et al., 1997; Ding, 2007).

Early studies on the mechanism of MJO suggest that this oscillation is a Kelvin wave forced by convective heating through the wave-CISK (conditional instability of the second kind) mechanism, but the so-derived MJO modes prefer the shortest wavelength (Wang, 1988) and the speed of propagation is too fast. The introduction of cumulus friction (Chang, 1977), conditional heating (Lau and Peng, 1987), and the inclusion of the wind-induced surface heat exchange (WISHE) feedback (Emanuel, 1987; Neelin et al.,

Supported by the United States National Science Foundation (AGS-1106536) and Office of Naval Research (N00014-1210450), China National Natural Science Foundation (41375095), and China Meteorological Administration Special Public Welfare Research Fund (GYHY201306032). This is SOEST contribution number 9066 and IPRC contribution number 1040.

*Corresponding author: timli@hawaii.edu.

[1] More complete reviews of the MJO/ISO can be found in Madden and Julian (1994), Lau and Waliser (2005), Zhang (2005), and Waliser (2006).

1987; Li et al., 2002) slow down the speed in idealized models. However, climate model simulations still produce shorter periods and weaker signals of MJO than observations (Lau and Lau, 1986; Slingo et al., 1996, 1999; Lin et al., 2006). Further inclusion of a boundary layer frictional effect (Wang, 1988; Wang and Li, 1994) results in a vertical structure similar to the observed (Hendon and Salby, 1994; Jones and Weare, 1996; Maloney and Hartmann, 1998, Chao and Chen, 1999; Moskowitz and Bretherton, 2000; Sperber, 2003). Studies also pointed out the role of air-sea interactions (e.g., Li and Liao, 1996; Flatau et al., 1997; Hendon and Glick, 1997; Lau and Sui, 1997; Shinoda and Hendon, 1998; Wang and Xie, 1998; Waliser et al., 1999; Kemball-Cook and Wang, 2001; Fu et al., 2003; Stephens et al., 2004; Maloney and Sobel, 2004; Zheng et al., 2004; Lin et al., 2011) and multi-scale interactions (e.g., Nakazawa, 1988; Grabowski, 2001; Majda and Biello, 2004; Moncrieff, 2004; Biello and Majda, 2005; Khouider and Majda, 2006; Biello et al., 2007) in the MJO.

MJO exhibits pronounced seasonality in its intensity (Madden, 1986), frequency (Hartmann et al., 1992), and movement (Wang and Rui, 1990a; Wu et al., 2005). In boreal winter, MJO is dominated by eastward propagation along the equator, but in boreal summer the eastward propagating mode substantially weakens, whereas northward propagation prevails in the Indian monsoon region (Yasunari, 1979, 1980; Hartmann and Michelsen, 1989; Gadgil and Srinivasan, 1990; Gautier and DiJulio, 1990) and the northwestward propagation prevails over the western North Pacific (WNP) (Murakami, 1980; Lau and Chan, 1986; Knutson and Weickmann, 1987; Nitta, 1987; Chen and Murakami, 1988; Hsu and Weng, 2001; Kemball-Cook and Wang, 2001). Nowadays, MJO mainly refers to oscillations along the equator, while ISO contains a wider range of frequency and includes oscillations propagating along and off the equator (Salby et al., 1994; Annamalai et al., 1999; Matthews, 2000; Mo, 2000; Annamalai and Slingo, 2001; Myers and Waliser, 2003; Jones et al., 2004a, b, c; Lau and Waliser, 2005). In this paper, we will refer to both, following the literatures cited.

MJO exhibits a multi-scale characteristic. Nakazawa (1988) showed that MJO is organized by clouds with scales from individual cumulus, mesoscale convective systems (MCS), to super cloud clusters (SSC). As it propagates eastward from the Indian Ocean (IO) to the western Pacific, MJO interacts with many weather and climate systems (Liebmann et al., 1994; Mo, 2000; Vecchi and Harrison, 2002; Jones et al., 2004a, b). The tropical IO and WNP are regions of enhanced MJO variability in boreal summer. These regions, not by coincidence, are also regions with most active synoptic-scale variability (SSV) including synoptic wave train and tropical cyclone (TC) activity (Lau and Lau, 1990; Liebmann et al., 1994; Hartmann and Maloney, 2001; Maloney and Dickinson, 2003; Straub and Kiladis, 2003; Batstone et al., 2005). It is well known that MJO exerts a large-scale control on SSV (Hendon and Liebmann, 1994; Maloney and Hartmann, 1998, 2000a, b; Straub and Kiladis, 2003). Some diagnostic studies suggested that barotropic energy conversion between the MJO flow field and higher-frequency eddies was responsible for latter's growth (Sobel and Maloney, 2000; Hartmann and Maloney, 2001; Maloney and Hartmann, 2001; Maloney and Dickinson, 2003). Maloney and Hartmann (1998, 2000a, b) suggested that MJO westerlies may set up favorable conditions for TC development by inducing cyclonic low-level vorticity and near-zero vertical wind shear. Using wave accumulation as a precondition for TC genesis, Sobel and Maloney (2000) found a relationship between TC genesis and MJO. They concluded that the wave activity convergence associated with tropical depression-type disturbances is stronger during the active phase of MJO.

Compared with the MJO impact on SSV, the synoptic-scale feedback to MJO has received less attention (Batstone et al., 2005). While MJO exerts a large-scale control on SSV, it is not clear how and to what extent the integrated effect of synoptic-scale (including TC) activity may further feed back to MJO. Krishnamurti et al. (2003) speculated that about 30%–50% of the total surface heat flux on the MJO timescale might come from the interaction of MJO with other timescales. Biello and Majda (2005), Biello

et al. (2007), and Majda and Stechmann (2009) suggested that the synoptic-scale momentum and temperature flux convergences may modulate the large-scale MJO circulation.

Currently, there is a gap in forecast skill between short-range (less than a week) weather and long-range (monthly or seasonally) climate prediction. MJO is a major predictability source for extended-range (10–30-day) forecast. Accurate prediction of MJO and associated intraseasonal variability in the tropics and extratropics is crucial for bridging the gap. Most of current operational models, however, have low skills in predicting MJO (Kim et al., 2009). It is not clear to what extent this is attributed to shortcomings in model physics, or the unpredictable component that is determined to a large extent by atmospheric chaotic behaviors (Sperber and Palmer, 1996; Goswami, 1998; Waliser et al., 2003). Our current knowledge in understanding MJO dynamics is limited. Revealing the dynamics of MJO including its propagation and initiation mechanisms will not only advance our current understanding of the tropical low-frequency dynamics but also on a long run improve our capability of prediction of intraseasonal variations of the global atmosphere and ocean so that the current gap between short-range weather forecast and seasonal climate prediction will be bridged.

This review paper describes what advancement we have made in recent years in understanding MJO dynamics, with a special focus on mechanisms related to MJO eastward propagation, planetary zonal scale selection, seasonality, initiation, and multi-scale interactions. The rest of the paper is organized as follows. In Section 2, the structure and physical processes relevant to MJO eastward propagation are described. In Section 3, a modeling result related to MJO planetary scale selection is presented. In Section 4, key processes responsible for the summer-winter contrast in MJO propagation behavior are discussed. In Section 5, observed precursor signals and physical processes responsible for MJO convection initiation in the western IO are described. In Section 6, MJO multi-scale interaction processes are discussed. Finally, a summary is given in Section 7.

2. MJO eastward propagation

The most striking feature in term of MJO structure is that it has a horizontal pattern of Kelvin-Rossby wave couplet (Wang and Rui, 1990b; Hendon and Salby, 1994; Wang and Li, 1994) and a vertical tilting in specific humidity and vertical motion fields (Sperber, 2003; Kiladis et al., 2005). Consistent with the tilting of vertical motion is the phase leading of planetary boundary layer (PBL) convergence with respect to MJO convection (e.g., Wang and Li, 1994; Maloney and Hartmann, 1998). While the previous studies have identified the zonal asymmetry of PBL moisture and convergence, the quantitative examination of causes of the phase leading and its role in eastward propagation remained absent until recently.

2.1 Observed three-dimensional structure of MJO

Using the ECMWF reanalysis (ERA-40), Hsu and Li (2012) examined the structure and evolution characteristics of the MJO over the tropical Indian Ocean-western Pacific warm pool region. Figure 1 illustrates the composite zonal-vertical distribution of 20–80-day filtered moisture field and its phase relationship with the MJO convection (when it is located in the eastern equatorial Indian Ocean). While in the mid troposphere the maximum moisture anomaly is co-located with the MJO convection, in the PBL there is a clear zonal asymmetry in the perturbation moisture field; that is, a positive (negative) center is located to the east (west) of the OLR center. Because of this asymmetry, the maximum moisture content line tilts eastward and downward. This moisture tilting feature is consistent with previous studies (e.g., Sperber, 2003; Kiladis et al., 2005).

The circulation anomalies at 200 and 850 hPa associated with the MJO convection over the eastern equatorial Indian Ocean (EIO) are displayed in Fig. 2. It generally shows a baroclinic Rossby-Kelvin wave couplet structure in response to the MJO heating, similar to that described in Hendon and Salby (1994) and Salby et al. (1994). To the west of the MJO convection, there are two large-scale anticyclonic (cyclonic)

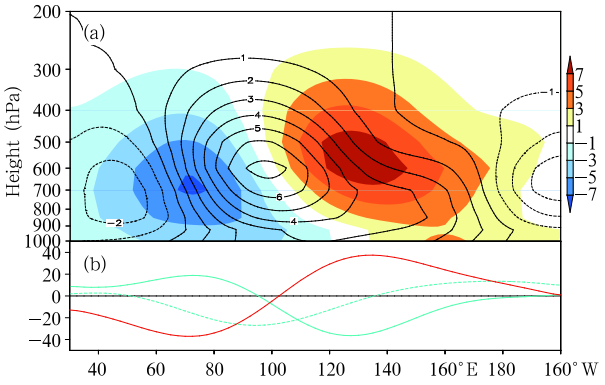

Fig. 1. (a) Zonal-vertical distributions averaged over 0°–10°S of 20–80-day filtered specific humidity (contour; 10^{-4} kg kg^{-1}) and specific humidity tendency (shading; 10^{-10} kg kg^{-1} s^{-1}). (b) Zonal distributions along 0°–10°S of 20–80-day filtered OLR (blue dashed line; W m^{-2}), OLR tendency (blue solid line; 10^{-6} W m^{-2} s^{-1}), and column-integrated specific humidity tendency (red line; 10^{-7} kg m^{-2} s^{-1}) during the active phase of MJO in the EIO. From Hsu and Li (2012).

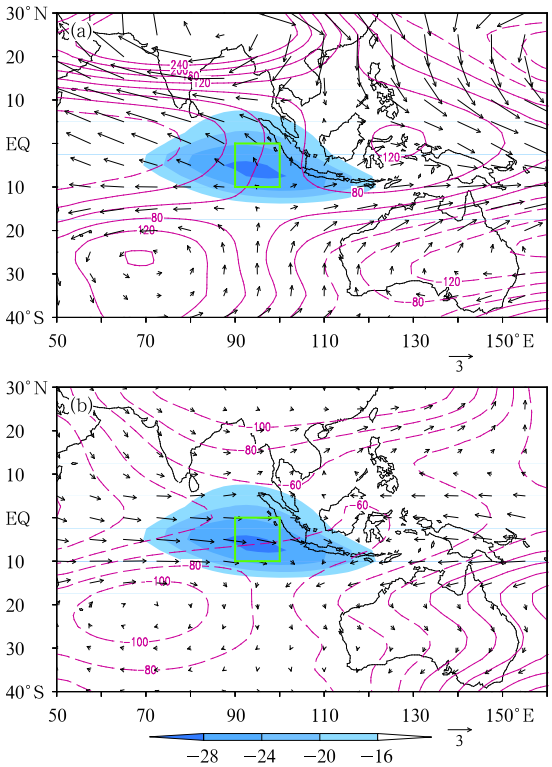

Fig. 2. Composites of 20–80-day filtered OLR (shading; W m^{-2}), geopotential (contour; m^2 s^{-2}), and wind fields (vector; m s^{-1}) at (a) 200 and (b) 850 hPa during the active phase of MJO in the EIO (green boxes). From Hsu and Li (2012).

Rossby wave gyres in the upper (lower) troposphere on both sides of the equator, accompanied with pronounced easterly (westerly) flows near the equator. To the east of the MJO convection, westerly (easterly) flows associated with the Kelvin wave response appear in the upper (lower) troposphere. Both the OLR center and the wave couplet structure shift slightly to the south of the equator, as the seasonal mean precipitation center in the region is primarily confined to the south of the equator (Li and Wang, 1994a). The circulation anomalies at 1000 hPa (figure omitted) in general resemble those at 850 hPa.

The zonal-vertical distributions of MJO circulations show a dominant first baroclinic mode vertical structure in the zonal and meridional wind fields (Fig. 3). At and to the west of the MJO convection, the westerly is pronounced in the lower-to-middle troposphere, while the easterly appears above 300 hPa. The maximum westerly appears around 850 hPa, and the zonal wind tilts westward with height. A similar tilting is found to the east of the MJO convection (Fig. 3a). A northerly (southerly) flow is observed in the vicinity of the MJO convection in the lower (upper) troposphere (Fig. 3b). As shown in the following, this meridional wind plays a role in anomalous moisture advection. While the strongest upward motion appears in the middle troposphere and is in phase with the OLR minimum center (90°–100°E), at top of the PBL the ascending anomaly tends to prevail to the east of the MJO convection (Fig. 3c). As a result, the vertical motion associated with MJO also tilts eastward as height decreases. The asymmetry of the vertical motion at top of the PBL is dynamically consistent with the divergence field at the PBL, which also reveals a remarkable zonal asymmetry with a convergence (divergence) appearing to the east (west) of the MJO convection (Fig. 3d).

2.2 A moisture budget diagnosis

To reveal the cause of the moisture asymmetry, a vertical (1000–700 hPa) integrated MJO moisture budget analysis is performed over the PBL moistening region. The moisture tendency is determined by the sum of horizontal and vertical moisture advections

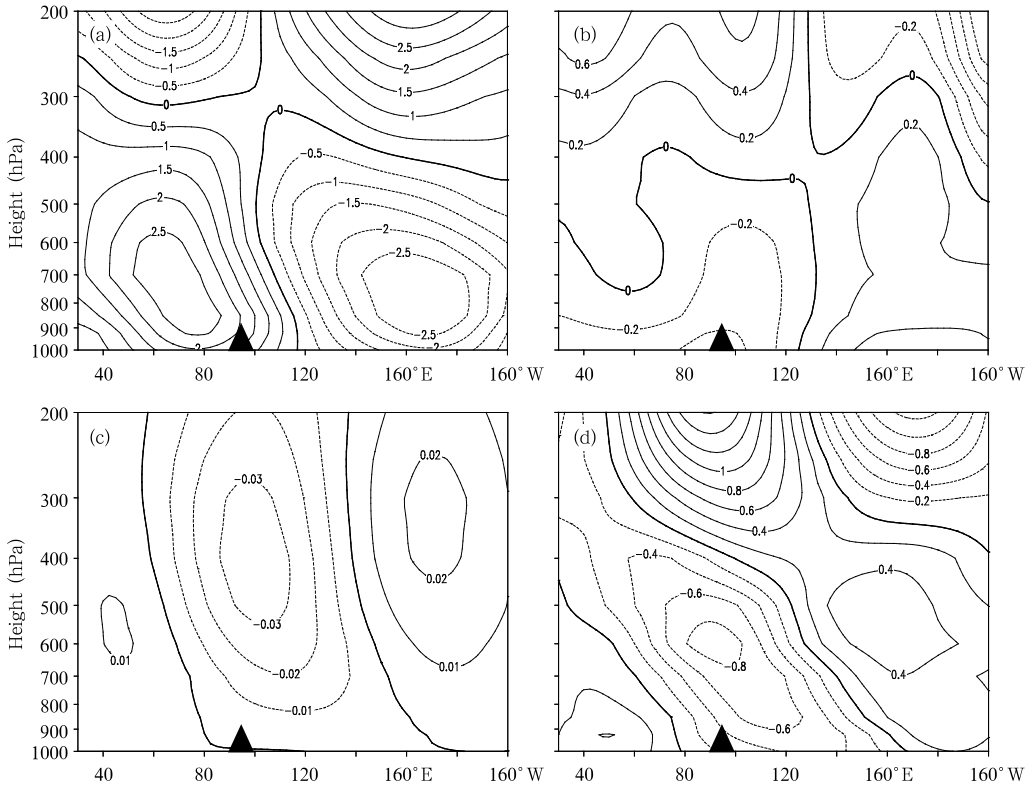

Fig. 3. Zonal-vertical distributions averaged along 0°–10°S of 20–80-day filtered (a) zonal wind (m s^{-1}), (b) meridional wind (m s^{-1}), (c) vertical velocity (Pa s^{-1}), and (d) divergence (10^{-6} s^{-1}) during the MJO active phase in the EIO. The triangles indicate the center of MJO convection. From Hsu and Li (2012).

and the atmospheric apparent moisture sink, Q_2 (Yanai et al., 1973).

$$\frac{\partial q}{\partial t} = -\boldsymbol{V} \cdot \nabla q - \omega \frac{\partial q}{\partial p} - \frac{Q_2}{L}, \tag{1}$$

where q is the specific humidity, t is the time, $\boldsymbol{V}$ is the horizontal wind vector, ∇ is the horizontal gradient operator, p is the pressure, ω is the vertical pressure velocity, Q_2 is the atmospheric apparent moisture sink, and L is the latent heat of condensation. Each term in Eq. (1) is applied with a 20–80-day filtered operator, averaged from 1000 to 700 hPa. Figure 4 shows the contribution from each of the moisture budget terms. The largest positive contribution is the vertical moisture advection term. The cause of the positive vertical advection is primarily due to the advection of the mean moisture by anomalous ascending motion, the latter of which is associated with the PBL convergence. In addition to the convergence effect, the horizontal moisture advection also contributes to the PBL moistening, although its magnitude is five times smaller than the vertical moisture advection term. The Q_2 term tends to reduce the moistening in the lower troposphere. The negative value of the Q_2 term in PBL (1000–700 hPa) results from the shallow convection induced pre-

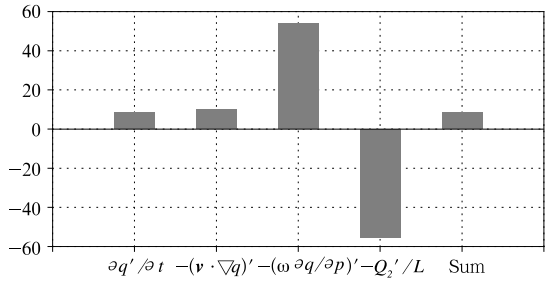

Fig. 4. PBL (1000–700 hPa) integrated intraseasonal moisture budget terms over PBL moistening region (0°–10°S, 130°–150°E). From left to right: observed specific humidity tendency, horizontal moisture advection, vertical moisture advection, latent heating, and sum of the advection and heating terms. Unit is 10^{-7} kg m^{-2} s^{-1}. From Hsu and Li (2012).

cipitation and the reduction of the surface evaporation ahead of MJO convection.

The leading term in the MJO moisture advection is the advection of the mean moisture by the MJO flow. The second leading term in the moisture advection is the anomalous moisture advection by the mean flow.

2.3 Mechanism for the eastward propagation

Figure 1 illustrates that while the mid-tropospheric moisture anomaly is approximately in phase with the MJO convection, there is a clear zonal asymmetry in the PBL moisture field. A positive (negative) specific humidity center is located to the east (west) of the OLR center.

To demonstrate how the PBL moisture asymmetry affects the MJO growth and evolution via atmospheric destabilization, the vertical profile of the intraseasonal equivalent potential temperature was examined. The equivalent potential temperature depends on both the specific humidity and temperature profiles of actual atmosphere. If a layer of air mass is initially moist but unsaturated and within the layer $\partial\theta_e/\partial z < 0$, we call the layer of the atmosphere being potentially (or convectively) unstable. If such a layer is brought to saturation by sufficient lifting, the whole layer becomes actually unstable (Holton, 1992; Emanuel, 1994). The occurrence of deep convection (such as thunderstorm) is often preceded by a period when the atmosphere is potentially unstable (Houze, 1993).

It is noted that a significant increase of low-level equivalent potential temperature occurs, consistently with PBL moistening to the east of the MJO convection. If defining a convective instability parameter as the difference of equivalent potential temperature between the PBL (850–1000 hPa) and the mid troposphere (400–500 hPa), one may find that the atmosphere is more (less) potentially unstable to the east (west) of the MJO convective center. Therefore, a phase leading of a positive low-level moisture anomaly may set up a relatively unstable stratification and generate a favorable environment for potential development of new convection to the east of the MJO center.

The westward tilting of moisture with height to the east of the convection implies that for an observer at a fixed location, the moisture precursor signal first appears at the low level, and then moves upward. This is consistent with the fact that shallow convection and cumulus congestus clouds appear prior to MJO deep convection (Johnson et al., 1999; Kikuchi and Takayabu, 2004; Benedict and Randall, 2007). The shallow convection transports moisture upward to moisten the mid troposphere, leading to the onset of deep convection.

2.4 Processes responsible for phase leading of PBL convergence

The moisture budget diagnosis above shows that a dominant moistening process in the PBL is the vertical advection of mean moisture by anomalous ascending motion. Since the anomalous ascending motion is related to PBL convergence, a key question becomes what causes the phase leading of the PBL moisture ahead of the MJO convection?

Figure 5 is a schematic diagram illustrating key processes that contribute to the phase leading of the boundary-layer convergence. Firstly, the mid-tropospheric heating associated with MJO deep convection induces a baroclinic free-atmosphere response, with a Kelvin (Rossby) wave response to the east (west) of the convective center. The anomalous low pressure at top of the PBL associated with the Kelvin wave response may induce a convergent flow in the boundary layer, while a PBL divergence may occur to the west of the convective center between two Rossby wave gyres. Thus, the first convergence-generation process is associated with the mid-tropospheric heating and equatorial wave responses to the heating. The second generation process is associated with the SSTA forcing. As a warm SSTA is generated to the east of the MJO convection, the warm SSTA may drive boundary layer flows through induced hydrostatic effect on sea level pressure (Lindzen and Nigam, 1987). Therefore, the convergence in the atmospheric boundary layer may be connected to the underlying positive SST anomaly and associated SSTA gradients to the east of the MJO convection.

To examine quantitatively the relative roles of the SSTA gradient induced pressure gradient force and

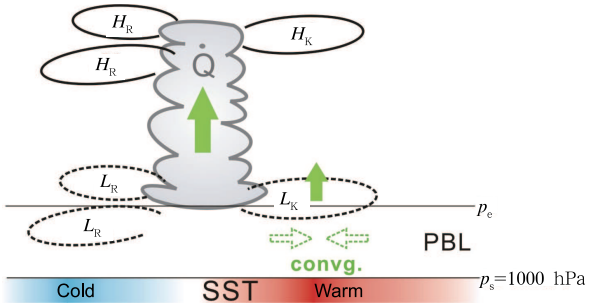

Fig. 5. Schematic diagram illustrating how the boundary layer convergence is controlled by free-atmospheric heating induced wave response and a warm SST anomaly induced by air-sea interaction. Cloud stands for the MJO convection. Solid (dashed) gyres with H_K (L_K) and H_R (L_R) indicate the high (low) pressure anomaly associated with Kelvin and Rossby wave response to the convection, bottom shadings denote the positive and negative SST anomalies respectively, solid arrows indicate the anomalous ascending motion, dashed arrows represent the boundary layer convergence, and p_s and p_e are pressure levels at the bottom and top of the PBL respectively. From Hsu and Li (2012).

the heating induced free-atmospheric wave dynamics in determining the PBL convergence, we diagnose the boundary-layer momentum budget equation developed by Wang and Li (1993). The PBL momentum equation (2.21) in Wang and Li (1993) states

$$f\boldsymbol{k}\times\boldsymbol{V}'_{\rm B}+E\boldsymbol{V}'_{\rm B}=-\nabla\phi'_{\rm e}+\frac{R}{2}\frac{(p_{\rm s}-p_{\rm e})}{p_{\rm e}}\nabla T'_s, \qquad (2)$$

where a prime denotes the MJO-scale variable, f is the Coriolis parameter, $\boldsymbol{k}$ is the unit vector in the vertical direction, $\boldsymbol{V}_{\rm B}$ denotes the vertically averaged horizontal wind in the boundary layer, ∇ is the horizontal gradient operator, $\phi_{\rm e}$ denotes the geopotential at the top of the boundary layer, R is the gas constant of air, $p_{\rm s}$ and $p_{\rm e}$ are pressures at the bottom and top of the PBL, respectively, $T_{\rm s}$ is the surface temperature, and E is the friction coefficient and is equal to 10^{-5} $\rm s^{-1}$. The first term on the right hand side of Eq. (2) represents the free-atmospheric wave effect. The second term on the right hand side of Eq. (2) represents the SSTA forcing effect. To test the sensitivity of the result to the boundary layer depth, two different PBL depths, 1000–850 hPa and 1000–700 hPa, are applied.

The diagnosis of each term in Eq. (2) using the ERA40 reanalysis data shows that the free atmospheric wave effect in response to the MJO heating plays a major role in determining the boundary-layer convergence. It accounts for 90% and 75% of the total boundary layer convergence in the case of $p_{\rm e}$= 850 and $p_{\rm e}$= 700, respectively. The warm SST anomaly induced by decreased latent heat flux (LHF) ahead of MJO convection, on the other hand, also plays a role. It contributes about 10%–25% to the observed boundary layer convergence. Since the PBL convergence is a major factor affecting the moisture asymmetry, the result above suggests that both the heating induced equatorial wave response and the underlying SSTA contribute to the eastward propagation of MJO.

2.5 Discussion

Based on the diagnosis of an atmospheric general circulation model, Maloney (2009) (hereafter M09) found that the horizontal advection dominates the positive tendency of column-integrated moist statistic energy (MSE) ahead of the MJO precipitation. However, the positive MSE tendency induced by the horizontal moisture advection is to a large extent offset by the surface LHF. Furthermore, the MSE or moisture budget analysis performed in M09 was based on the vertical integration in atmospheric column. However, as shown in Hsu and Li (2012), the column-integrated moisture tendency primarily reflects the moisture change in the middle troposphere, which is approximately symmetry to the convection. In this case, mid-tropospheric perturbation moisture cannot cause the eastward propagation. Given that the major asymmetry occurs in the PBL moisture field and that the PBL moistening occurs prior to the mid-tropospheric moistening, it is conceivable that the PBL moisture asymmetry is critical for preconditioning of subsequent development of atmospheric convection.

M09 also pointed out that a weakening of transient eddy moisture transport is a major contributor of moistening ahead of the MJO precipitation center. However, this model result is not supported by the observational analysis of Hsu and Li (2012). In a theoretical work by Sobel and Maloney (2013), a verti-

cally integrated moist static energy quantity was used, which neglected the effect of vertically tilted moisture structure. They emphasized the role of horizontal moisture advection (including eddy moisture transport) in the eastward propagation. As one can see from Fig. 4, horizontal advection does play a role. However, its magnitude is much smaller than the vertical advection. Some argued that the vertical advection should not be counted because it partially cancels out with the diabatic term. Such an argument is unphysical, because both the horizontal and vertical advection terms are adiabatic processes and they should be treated equally.

The critical role of the vertical advection in causing the moisture asymmetry and the eastward propagation can be clearly demonstrated from an aqua-planet simulation (with use of MRI AGCM) under a specified zonally uniform SST distribution. In a control simulation, MJO-like variability is reproduced in a world with pronounced background easterly flows at the equator. A diagnosis of the model output shows that PBL specific humidity leads to the MJO convection as it propagates eastward. A further diagnosis of the PBL moisture budget shows that the moisture leading is attributed to the vertical advection associated with PBL convergence. The horizontal moisture advection contributes negatively to the MJO propagation as the mean flows advect the perturbation moisture westward. The aqua-planet simulation clearly demonstrates the critical role of the vertical moisture advection (and associated anomalous PBL convergence) in causing the eastward propagation of MJO.

To demonstrate the importance of the moisture asymmetry, we carried out a sensitivity experiment using the aqua-planet model in which we force the model specific humidity toward a zonal mean background moisture field while allowing the divergence being asymmetric. The sensitivity experiment result shows that the MJO-like variability disappears in this idealized setting. This indicates that the moisture asymmetry, not the convergence asymmetry, is critical for MJO propagation.

The sensitivity experiment above and the observational study of Hsu and Li (2012) emphasized importance of zonal asymmetry of the perturbation moisture. One may wonder why the eastward propagation of MJO existed in the 2.5-layer model of Li and Wang (1994a) in which a perturbation moisture field was not considered (in the model only the background mean specific humidity was specified). We believe that the eastward propagation in the model is attributed to an idealized convective heating scheme. In the model the heating is proportional to vertically integrated moisture convergence, which consists of the lower-tropospheric moisture convergence and the PBL moisture convergence. The former is in phase with the MJO convection and primarily responsible for reducing the atmospheric stratification. The latter leads the MJO convection and thus is responsible for both the propagation and growth of the low-frequency perturbation. Given that a parameterized heating always appears to the east of the MJO convection, such a heating would drag the system eastward.

3. MJO planetary-scale selection

An outstanding question for MJO is why the oscillation prefers a planetary zonal scale. There have been a number of theoretical studies aimed at addressing this scale selection issue. Chang (1977) proposed that the MJO can be represented by convectively driven equatorial Kelvin waves. However, the wave-CISK mechanism prefers the most unstable growth at a shorter zonal wavelength. Lau and Peng (1987) and Chang and Lim (1988) demonstrated in numerical models that the Kelvin wave with a zonal wavenumber-1 structure is selectively amplified when a positive-only condensational heating is applied. Using a linear 2.5-layer model that consists of a two-level free atmosphere and a well mixed PBL, Wang (1988) showed that the instability of MJO may arise from the boundary layer friction-induced moisture convergence. A preferred planetary zonal wavelength may be derived when a low-frequency (40–50-day) period is specified. This did not solve the scale selection problem because the temporal and spatial scales are related. Goswami and Rao (1994) presented a mechanism for selective excitation of the equatorial Kelvin wave at the period of 30–50 days when a time lag be-

tween the convection and the heating is assumed.

While many numerical studies pointed out the importance of the nonlinear positive-only heating in the MJO scale selection, it is not clear how the nonlinear heating leads to the planetary scale selection. This motivates us to address this issue in the current study.

The model used in this study is the 2.5-layer atmosphere model of Li and Wang (1994a) and Wang and Li (1994). The governing equations may be written as:

$$\begin{aligned} &\frac{\partial \boldsymbol{V}}{\partial t} = -f\boldsymbol{k}\times\boldsymbol{V} - \nabla\phi, \\ &\frac{\partial \phi}{\partial t} + C_0^2(1-\delta I)\nabla\cdot\boldsymbol{V} = C_0^2(\delta B - 1)\nabla\cdot\boldsymbol{V}_{\rm B}, \\ &E\boldsymbol{V}_{\rm B} + f\boldsymbol{k}\times\boldsymbol{V}_{\rm B} = -\nabla\phi, \end{aligned} \tag{3}$$

where $\boldsymbol{V}$ and $\boldsymbol{V}_{\rm B}$ denote the lower-tropospheric and boundary-layer winds, ϕ denotes the lower-tropospheric geopotential height, f, C_0, and E are the Coriolis parameter, first-baroclinic mode gravity wave speed, and Ekman frictional coefficient, and I and B are convective heating coefficients contributed by the wave convergence and boundary layer frictional convergence, respectively (Wang, 1988).

The condensational heating rate in the middle troposphere is proportional to the vertically integrated moisture convergence,

$$Q'_m = \frac{\delta b L_c}{\Delta p}\left[-\omega'_m(\bar{q}_2 - \bar{q}_1) - \omega'_e(\bar{q}_e - \bar{q}_2)\right], \tag{4a}$$

where δ is a SST-dependent conditional heating coefficient (Wang and Li, 1993); $\bar{q}_1$, $\bar{q}_2$, and $\bar{q}_e$ denote the mean specific humidity field in the upper troposphere, lower troposphere, and PBL, respectively; the background humidity field is the function of the surface humidity and decays exponentially with height (Wang, 1988); ω'_m and ω'_e are the MJO-scale vertical velocities in the middle troposphere and at the top of PBL, respectively. The model covers a domain of (40°S–40°N, 0°–360°) with a horizontal resolution of 5° longitude by 2° latitude. A constant SST of 29℃ is specified, and the heating is separated into a nonlinear and linear heating. For the nonlinear heating (i.e., conditional positive-only heating), δ is unity at the vertically integrated moisture convergence region and zero at the vertically integrated moisture divergence region.

The role of the nonlinear heating on MJO scale selection is revealed by conducting two sets of numerical simulations from the two-and-half layer model. In the first set of experiments, a linear heating ($\delta \equiv 1$) is specified. In the second set, a nonlinear, positive-only heating is specified. For each set of experiments, 15 runs are conducted, each of which has the same initial Kelvin wave structure but a different zonal wavenumber of 1, 2, …, and 15, respectively. Each initial perturbation has the same amplitude and the same first baroclinic mode vertical structure.

3.1 Simulations with a linear heating

As predicted from a linear eigenvalue analysis, the numerical simulations from the first set of experiments show the exponential growth of the MJO perturbation as it propagates eastward along the equator. For the linear heating case, the model is integrated for five days. Because different wave components do not interfere with each other in a linear system, the perturbation keeps its initial wavenumber. Since the evolution and propagation of the perturbations bear similar features for all wavenumbers, only the model simulation from the initial wavenumber 5 perturbation case is shown. Figure 6a shows the time evolution of the lower tropospheric zonal wind along the equator. The perturbation moves eastward and grows while keeping the initial wavenumber 5 structure. There is no generation of the planetary zonal scale perturbation.

To calculate the growth rate for each wavenumber, a Fourier decomposition is applied to the model zonal wind field. Note that the perturbation always retains its initial wavenumber under the linear heating. Although all initial perturbations grow under the linear heating, the growth rates at different zonal wavenumbers are different. The growth rate at each wavenumber is calculated based on the time series of the Fourier coefficient of the corresponding zonal wavenumber. Figure 7a shows the dependence of the growth rate on the wavenumber. Note that the maximum growth rate appears at wavenumber 6. Weaker growth rates in higher wave number were attributed to use of diffusion terms in the model, which suppress

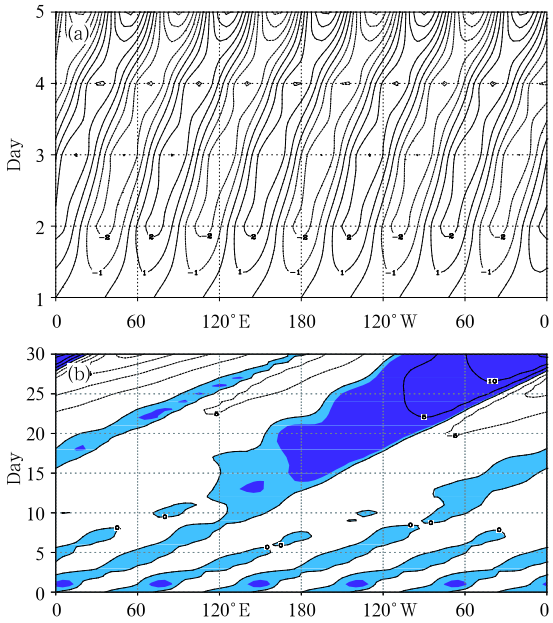

Fig. 6. Time-longitude cross-section of the equatorial zonal winds from the 2.5-layer model under the (a) linear and (b) nonlinear heating. An initial wavenumber 5 perturbation is specified. In (a), the contour interval is 1 m s^{-1}, with solid and dashed contours denoting the westerly and easterly, respectively. In (b), the contour interval is 5 m s^{-1} and the shading corresponds to the westerly wind. From Li and Zhou (2009).

mostly short wavelength perturbations. The numerical result indicates that the most unstable mode does not appear in the planetary zonal scale under the linear heating.

3.2 Simulations with a nonlinear heating

For the nonlinear, positive-only heating experiments, 15 runs with initial wavenumbers from 1 to 15 have been carried out, and for each run the model is integrated for 30 days. Figure 6b shows the simulated zonal wind field at the equator for the initial wavenumber 5 case. During the first 10 days, the perturbation remains the initial wavenumber 5 structure, while propagating eastward along the equator. After this adjustment period, the amplitude of the wavenumber 5 perturbation decays, while a wavenumber-1 perturbation starts to develop. By day 20, the equatorial zonal wind field is dominated by the planetary zonal scale.

The experiments with other initial wavenumbers show a similar result, this is, no matter what initial zonal wavenumbers are given, the nonlinear heating leads to a planetary zonal scale selection at the final stage. Figure 6b shows the growth rates at each run with different initial wave numbers. The wavenumber 1 perturbation grows fastest, indicating a planetary scale selection. The horizontal structure of the most unstable mode has a Kelvin-Rossby wave couplet pattern, similar to the observed (e.g., Hendon and Salby, 1994). The propagation speed of the couplet is slightly faster than the observed. The time to circulate around the globe is around 30–50 days, indicating the intraseasonal periodicity of the mode.

An additional experiment is carried out in which all the 15 wavenumbers with equal strength are input initially under the nonlinear heating. The evolution of the model zonal wind (figure omitted) shows a faster growing wavenumber-one component compared to that in Fig. 7b. For example, at day 30, the amplitude of the zonal wind is about 6 times greater. This experiment again demonstrates that given the equal strength wavenumbers 1–15 initially, the model favors the most unstable growth of the planetary zonal scale.

How does the nonlinear heating cause the planetary scale selection? Figure 8 is a schematic diagram illustrating how the scale selection process happens in

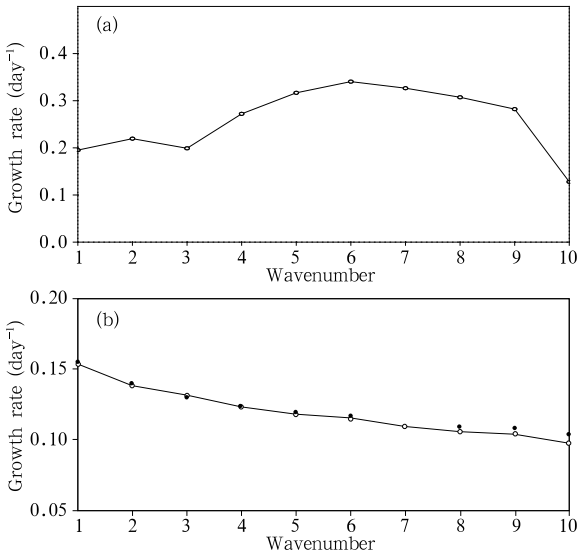

Fig. 7. Growth rates as a function of wavenumber derived from the 2.5-layer model simulations under the (a) linear (from Li and Zhou (2009)) and (b) non-linear heating.

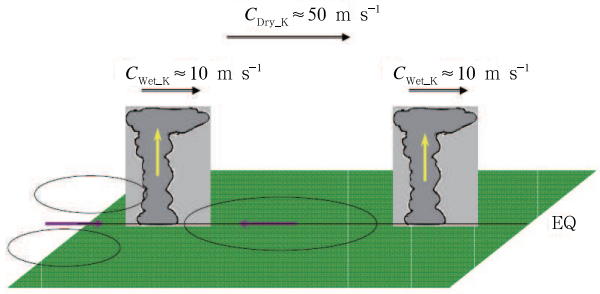

Fig. 8. Schematic diagram illustrating the role of the nonlinear heating in the MJO planetary zonal scale selection. From Li and Zhou (2009).

the model. It is primarily attributed to the distinctive phase speeds between the dry Kelvin wave and the moist Kelvin-Rossby wave couplet under the nonlinear heating. According to Gill (1980), convective heating at the equator may excite eastward-traveling Kelvin waves to its east. In the presence of the linear heating (i.e., $\delta \equiv 1$), the phase speed of the equatorial Kelvin waves, which is proportional to $\sqrt{1-\delta I}$ (Wang, 1988), remains the same for both the dry (suppressed convective) and wet (enhanced convective) regions. As a result, the dry and moist Kelvin waves propagate at the same speed so that dry and wet regions do not interfere with each other, no matter what the initial zonal wavenumber is. In the presence of the nonlinear, positive-only heating, the phase speeds of the dry Kelvin wave and the moist Kelvin-Rossby wave couplet are different since δ takes different values in the dry and wet regions. The phase speed of the dry Kelvin waves associated with descending motion (where $\delta = 0$) is much larger than that of the wet Kelvin-Rossby wave couplet associated with ascending motion (or low-level convergence where $\delta = 1$) (Wang and Li, 1994). Therefore, dry Kelvin waves, once excited by one convective branch, may "catch up" and suppress another convective branch to its east, as long as the zonal distance between the two neighboring convective branches is less than a critical distance.

This critical distance measures how far a dry Kelvin wave may propagate away from a forcing region under a realistic atmospheric dissipation/friction. According to Gill (1980), a maximum impact distance for the Kelvin waves depends on the phase speed of the dry Kelvin wave (50 m s^{-1}) divided by a Rayleigh friction/Newtonian damping coefficient. With a realistic dissipation coefficient, Gill (1980) showed a critical distance of about 160 longitude degrees. This implies that for perturbations with a wavelength shorter than the critical distance, the fast dry Kelvin wave may interfere and suppress the wet Kelvin-Rossby wave couplet convective branch ahead of it. Through this special "scale selection" process, shortwave perturbations are dissipated or "cut-off", while the planetary scale perturbations grow.

4. Winter-summer contrast in MJO propagation

The MJO exhibits distinctive propagation characteristics between boreal summer and winter (Wang and Rui, 1990a; Madden and Julian, 1994). While MJO in boreal winter is characterized by eastward propagation with maximum amplitude shifting slightly south of equator (Hendon and Salby, 1994; Maloney and Hartmann, 1998; Sperber, 2003; Kiladis et al., 2005; Hsu and Li, 2012), major convective branches associated with the MJO in boreal summer have a northward bifurcation over eastern IO before reaching the maritime continent (Lawrence and Webster, 2002; Jiang et al., 2004). Figure 9 shows the standard deviation of 20–80-day filtered rainfall anomalies and MJO propagation vectors in boreal winter and summer.

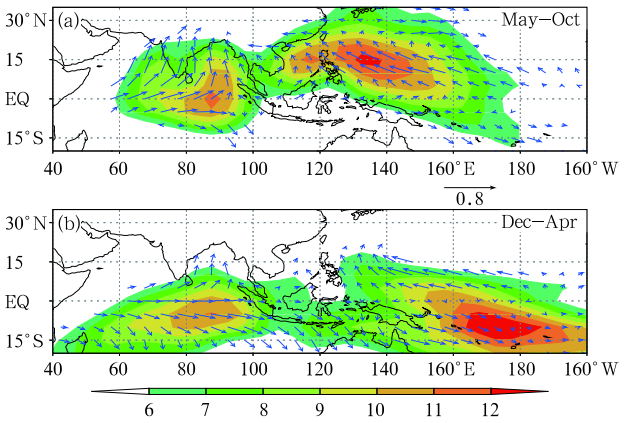

Fig. 9. The standard deviation of 20–80-day filtered CMAP rainfall anomalies (shaded) during 1979–1998 and propagation vectors for boreal (a) summer (May–October) and (b) winter (December–April).

Here, the propagation vectors are calculated based on the lead-lag correlation maps of localized intraseasonal rainfall centers. Focusing on strong MJO variance regions, one can see that major convective branches associated with MJO in northern winter are confined south of the equator and propagate eastward, whereas major convective activity associated with MJO in northern summer is confined north of the equator and propagate northward in northern IO and northwestward in WNP.

To examine how the maritime continent (MC) contributes to the MJO northward bifurcation, Zhu et al. (2010) conducted a set of idealized ECHAM5 T159 experiments. In the control experiment (CTL), the model is integrated for 11 yr with realistic land-sea mask. To examine the role of the MC on the MJO, a sensitivity experiment was designed in which the model setup was kept the same as CTL except that the MC land (10°S–10°N, 90°–160°E) was replaced by the ocean. SST in the original maritime continent grid is interpolated from the surrounding ocean points. This simulation is referred to as the no-maritime continent experiment (NOMC).

To focus on the northward propagation in the monsoon sector, Zhu et al. (2010) conducted a meridional wavenumber-frequency analysis between 10°S and 30°N, averaged for 10 boreal summers (from May to October) over the longitudinal domain of 65°–160°E. Figure 10 shows the wavenumber-frequency spectrum for the meridional propagating MJO modes based on the rain rate fields in the CMAP observation, CTL, and NOMC, respectively. In CTL, the northward-propagating ISO variance is considerably larger than that of the southward-propagating mode. The maximum spectrum appears at the period of 30–50 day and the wavelength of 4000 km. The corresponding northward phase propagation speed is about 1.2 m s^{-1}. The model simulation is consistent with the observation (Fig. 10a). Although a little weaker in MC, the gross pattern of MJO spectrum in NOMC is quite similar to that in CTL, implying that the existence of the maritime continent is not critical for northward bifurcation of MJO convection in boreal summer.

It is hypothesized that a key to the northward bifurcation of MJO convection in northern summer lies in the equatorial asymmetry of a thermal equator in the MC longitudes. In other words, it is the mean state asymmetry that controls MJO propagation. As we know, maximum mean ascending branch of local Hadley circulation lies over the warmest water at 15°N in northern summer (where the monsoon trough locates), while the descending branch of the local Hadley Cell appears at and south of the equator. This is in a great contrast to northern winter when the maximum convective branch of the local Hadley Cell appears at and slightly south of the equator. Such a mean state difference reflects clearly in PBL divergence and rainfall fields (Fig. 11).

How does the mean state affect the MJO propagation? Consider MJO as a convectively coupled Kelvin-Rossby wave couplet. In boreal winter, because maximum mean ascending motion and moisture are near the equator (within one Rossby radius of deformation), atmospheric moist Kelvin waves are unstable and grow faster than Rossby waves. As a result, Kelvin waves

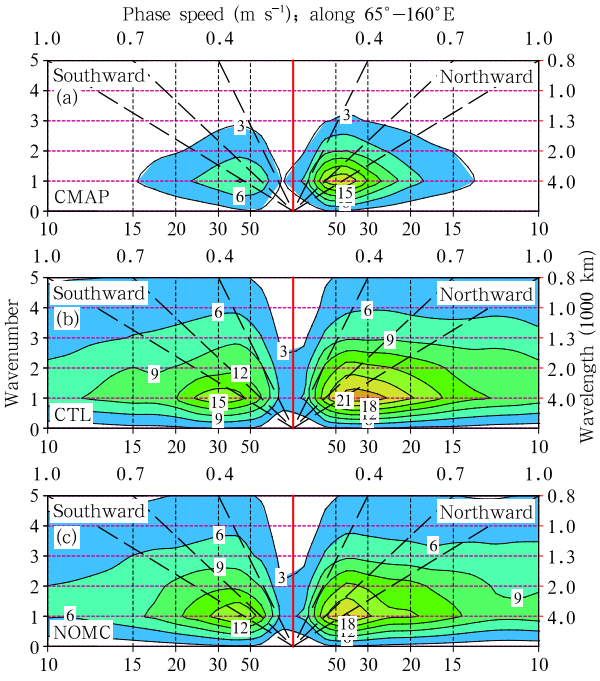

Fig. 10. The wavenumber-frequency spectrums for the meridional propagation mode averaged along 65°–160°E, calculated based on the rain rate fields from the (a) CMAP observation, (b) CTL, and (c) NOMC experiments, respectively. The contour interval is 2.0 (mm day^{-1})^2.

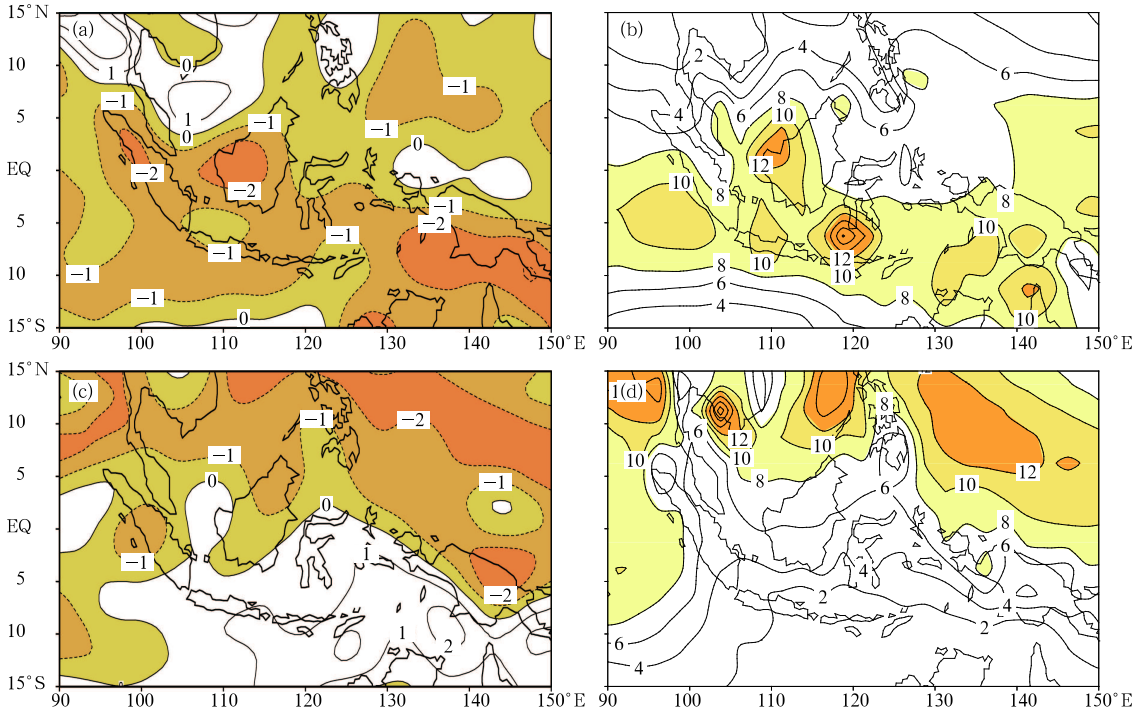

Fig. 11. Northern winter (DJF; a, b) and summer (JJA; c, d) mean PBL (averaged from 1000 to 850 hPa) divergence ($\times 10^{-6}$ s^{-1}) (a, c; derived from ERA40 reanalysis) and mean precipitation (b, d; derived from CMAP) fields.

dominate and MJO convection is confined near the equator. In boreal summer, because maximum mean ascending motion and moisture are located more than one Rossby radius of deformation away from the equator, atmospheric moist Kelvin waves stabilize due to the mean descending motion near the equator while Rossby waves become unstable. The suppressed convection near the equator causes the Kevin-Rossby wave couplet decoupled, and Rossby waves are emanated from the wave packet. Maximum convection appears off the equator, co-locating with Rossby gyres.

To demonstrate the mean flow effect, an eigenvalue analysis with use of the 2.5-layer model (shown in Eq. (3)) was conducted. For simplicity, atmospheric intraseasonal heating is assumed to be proportional to PBL moisture convergence, that is,

$$Q \propto \delta \cdot B(q_{\mathrm{e}}) \cdot \nabla \boldsymbol{V}_{\mathrm{B}}, \tag{4b}$$

where nonlinear heating coefficient δ is set to be 1 where the background SST is greater than 27°C and there is background PBL convergence, and to be 0 otherwise. The background surface air specific humidity in the model is determined from the SST according to an empirical formula shown in Li and Wang (1994b).

Figures 12a and 12b show the meridional distribution of specified background SST in boreal winter and summer. For simplicity, the boreal winter SST is assumed to be symmetric about the equator, while the boreal summer SST has a maximum amplitude right at one Rossby radius of deformation (non-dimensional $y = 1$). The influence of the mean flow convergence on the heating is not considered in the idealized SST distribution cases. Figures 12c–f show the eigenvalue analysis result. It is interesting to note that the equatorially asymmetric summer mean state leads to the decay of equatorial Kelvin waves but the growth of Rossby waves, whereas the equatorially symmetric winter mean state favors the growth of the Kelvin waves but the decay of Rossby waves.

Figures 13c and 13d illustrate the non-dimensional growth rate of the equatorial Kelvin and Rossby waves in the presence of realistic PBL moisture and divergence distributions averaged over the MC longitudes (shown in Figs. 13a and 13b). Similar to the above idealized cases, the equatorial Kelvin waves are unstable under the boreal winter mean state

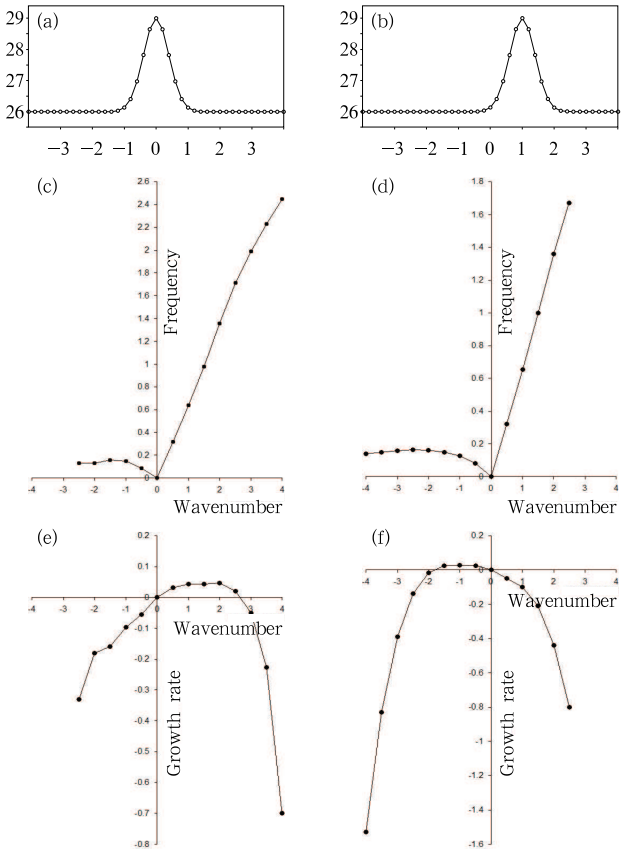

Fig. 12. Idealized background meridional SST distributions as a function of non-dimensional y in boreal (a) winter and (b) summer specified in a theoretic 2.5-layer model. Background surface air specific humidity is calculated based on the SST according to Li and Wang (1994b). Also shown are (c, d) non-dimensional frequency and (e, f) non-dimensional growth rate as a function of non-dimensional zonal wavenumber derived from the 2.5-layer model for boreal (c, e) winter and (d, f) summer.

while the Rossby waves become unstable under the boreal summer mean state. The theoretical model results prove the hypothesis that the marked northward shift of the thermal equator in northern summer is essential for the meridional bifurcation of MJO convection off Sumatra.

In addition to the northward shift of the thermal equator, the background easterly shear and meridional moisture distributions also contribute to the northward propagation of MJO convection in boreal summer over northern Indian Ocean and South China Sea (Jiang et al., 2004). The northward propagation can directly affect rainfall variability over the monsoon regions. In addition, MJO heating over the WNP and Indian monsoon regions can remotely affect midlatitudes through teleconnection (Kawamura et al., 1996; Ding and Wang, 2007; Pan and Li, 2008; Wang et al., 2013).

5. MJO initiation over the western equatorial Indian Ocean

An open question regarding its life cycle is how MJO is initiated over the western equatorial Indian Ocean (WIO). A widely accepted hypothesis is that MJO convection initiation arises from the circumnavigation of a preceding MJO event that travels around the global tropics (e.g., Lau and Peng, 1987; Wang and Li, 1994; Matthews, 2000, 2008; Seo and Kim, 2003). The promise behind the circumnavigating hypothesis is that the eastward-propagating MJO wave may trigger deep convection over moist and warm Indian Ocean after it passes the African continent, with

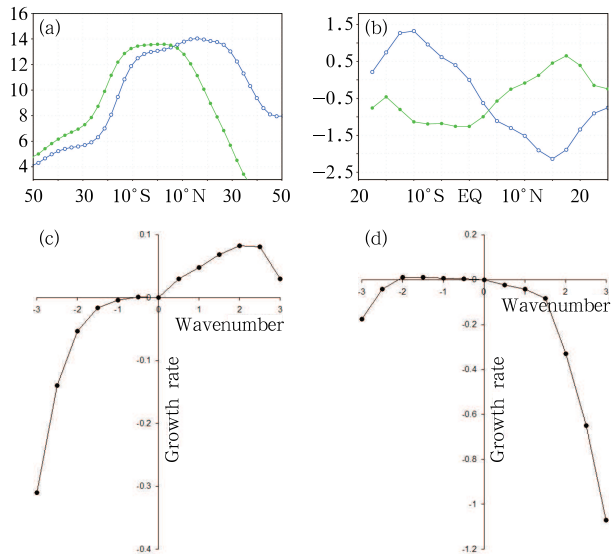

Fig. 13. Observed background (a) specific humidity (g kg^{-1}) at 900 hPa and (b) PBL divergence ($\times 10^{-6}$) fields averaged over 110°–140°E in boreal winter (the curve with dots) and summer (the curve with circles). Non-dimensional growth rate as a function of non-dimensional zonal wavenumber in the presence of the observed meridional distributions of background SST, specific humidity, and PBL divergence in boreal (c) winter and (d) summer.

possible topographic lifting effect (Hsu and Lee, 2005). In this scenario, the forcing from the upstream (west of the initiation region) holds a key for triggering new convection over the WIO. As demonstrated by Zhao et al. (2013), this circumnavigating process is not crucial for the initiation of most MJO events.

In addition to tropical forcing processes, MJO convection may be triggered by extratropical or midlatitude processes. For example, case studies by Hsu et al. (1990) and Ray et al. (2009) suggested that the midlatitude perturbations may propagate into the tropics and trigger MJO initiation over the WIO. However, large samples are needed in order to derive statistically robust signals.

5.1 Observed precursor signals associated with MJO initiation

Using 20-yr (1982–2001) observed OLR and ERA40 reanalysis data, Zhao et al. (2013) examined precursor signals associated with MJO convection initiation over the WIO. Figure 14 illustrates the composite evolution of OLR from day –9 to day 0 at a 3-day interval. Day 0 is referred to a time when MJO convection appears in the central equatorial IO. The OLR evolution maps reveal that the MJO convection was firstly initiated in the southwestern Indian Ocean, and then it propagates eastward. During its eastward journey, the convection is strengthened and shifts more toward the equator.

Based on the composite OLR evolution maps, the region of (20°S–0°N, 50°–70°E) is defined as the MJO convection initiation region. To reveal precursor signals associated with the convection initiation, Zhao et al. (2013) examined the time evolution of several key variables averaged over the region. Figure 15a presents the time evolution of the intraseasonal (20–90-day) OLR anomaly averaged over the initiation region. Note that the OLR anomaly transitions from a positive to a negative value at day –15. Consistent with the OLR transition is the switch of sign of the mid-tropospheric vertical motion, from an anomalous descending motion to an anomalous ascending motion (Fig. 15b). Thus, day –15 is regarded as the initiation date.

It is interesting to note that 7 days prior to the initiation date, a marked sign change of the specific humidity and temperature fields appears in the lower troposphere (Figs. 15c and 15d), that is, the lower-tropospheric specific humidity and temperature anomalies transition from a negative value to a positive value one week prior to the initiation date. The specific humidity perturbation is initially confined at low level and gradually penetrates into the middle troposphere. At day –15, the positive moisture anomaly has extended up to 500 hPa. The temperature perturbation, on the other hand, is primarily confined below

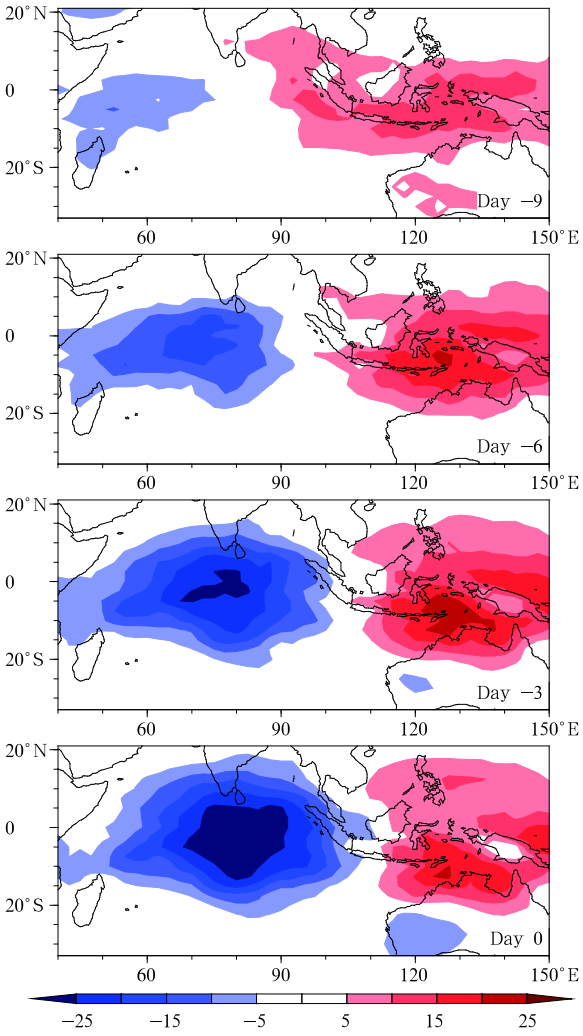

Fig. 14. Evolution of the composite OLR (W m^{-2}) pattern from day –9 to day 0 at a 3-day interval. The negative OLR represents enhanced MJO convection. Day 0 corresponds to a time when maximum MJO convection is located in the eastern equatorial IO. From Zhao et al. (2013).

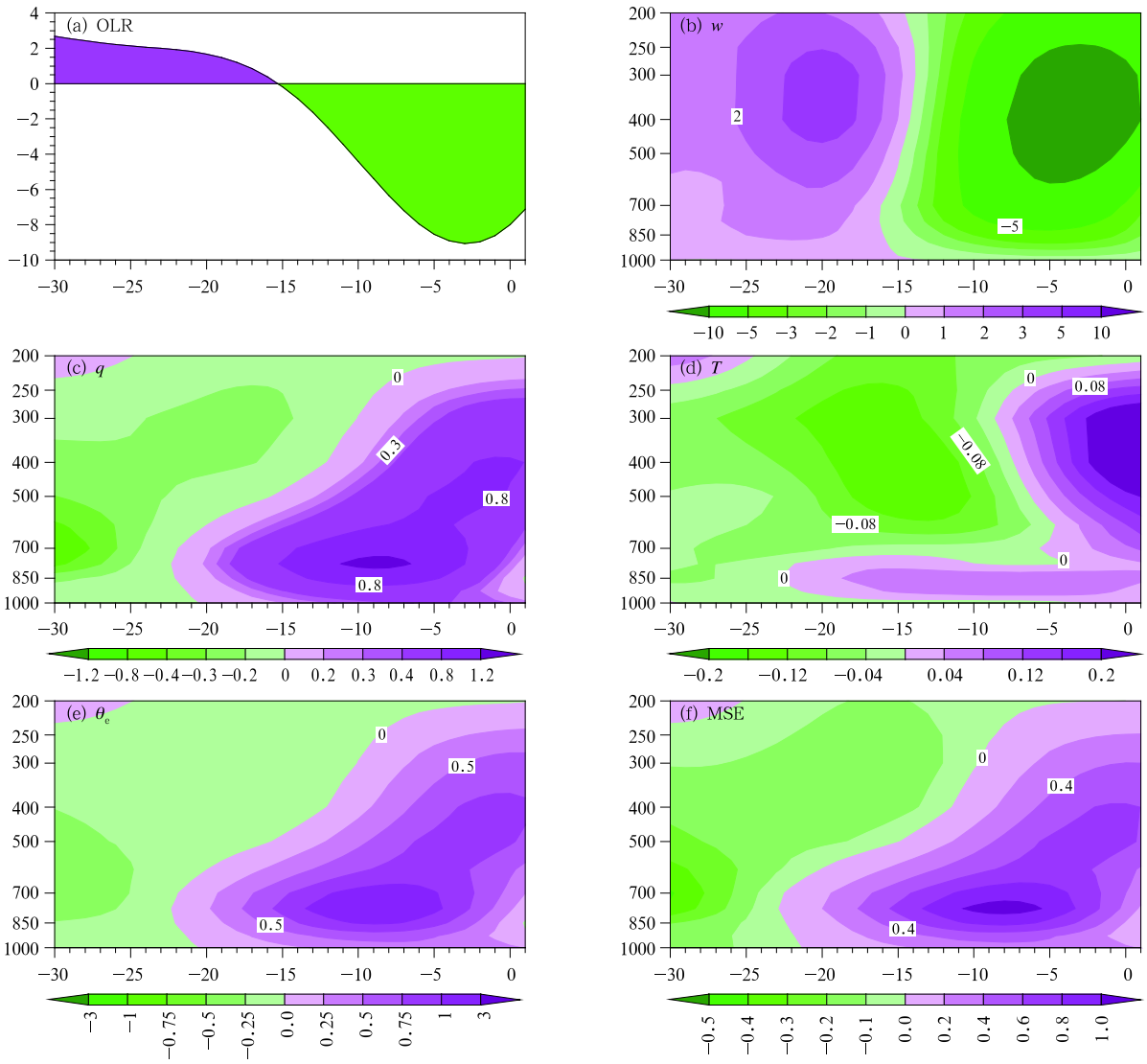

Fig. 15. Evolutions of (a) the composite intraseasonal OLR anomaly (W m^{-2}) and (b–f) vertical profiles of intraseasonal vertical velocity (w; 10^{-3} Pa s^{-1}), specific humidity (q; g kg^{-1}), temperature (T; K), equivalent potential temperature (θ_e; K), and moist static energy (MSE; K J kg^{-1}) fields averaged over the MJO initiation region (20°S–0°N, 50°–70°E).

700 hPa till day –8.

The marked increase of both the lower-tropospheric specific humidity and temperature leads to an increase of equivalent potential temperature (θ_e) and moist static energy (MSE) in the lower troposphere, as shown in Figs. 15e and 15f. The vertical time cross-section of θ_e shows that about one week prior to the initiation date, a positive θ_e perturbation appears in the lower troposphere. This positive perturbation intensifies rapidly while extending upward, closely following the specific humidity evolution.

The observational data analysis above indicates that lower-tropospheric moistening and warming prior to the convection initiation is crucial for the establishment of a convectively more unstable stratification. What physical processes contribute to the lower-tropospheric moistening and warming? To address this question, a vertically integrated (1000–700 hPa) intraseasonal moisture budget is diagnosed.

Figure 16 shows the moisture budget diagnosis result. It is clear that the positive moisture tendency during the initiation period (from day –25 to –15) is mainly attributed to the horizontal advection, while the vertical advection (due to subsidence and associ-

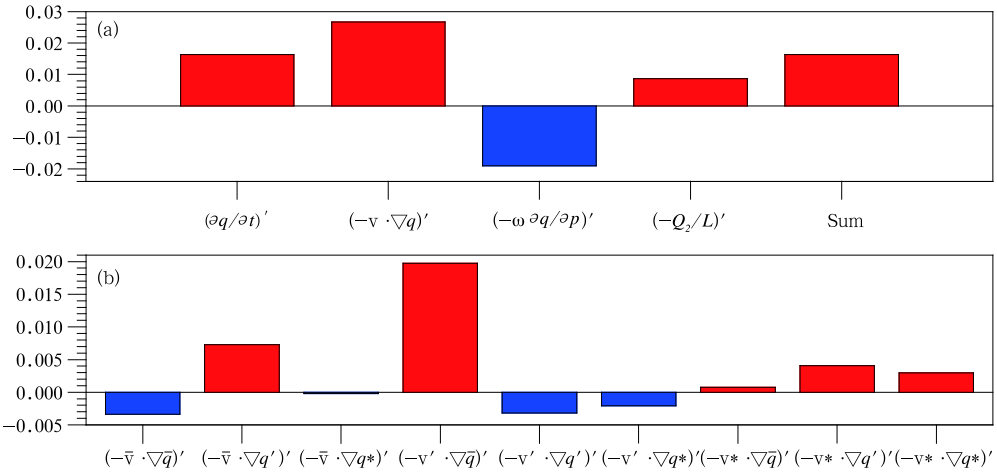

Fig. 16. (a) 1000–700 hPa integrated intraseasonal moisture budget terms averaged during the period of day –25 to day –15 over 20°S–0°N, 50°–70°E. From left to right: observed specific humidity tendency, horizontal moisture advection, vertical moisture advection, apparent moisture source, and sum of the last three terms. (b) Individual components of the horizontal moisture advection term. From Zhao et al. (2013).

ated divergence) is against the lower-tropospheric moistening. The result indicates that the lower-tropospheric moistening process during the MJO initiation is very different from that during its eastward propagation phase. In the latter case the lower-tropospheric moistening is primarily attributed to the vertical advection associated with PBL convergence (Hsu and Li, 2012).

The apparent moisture source term ($-Q_2/L$) plays a minor but positive role in the low-tropospheric moistening. This is because anomalous descending motion during the initiation period reduces the mean precipitation, leading to less condensational heating and thus more moisture retained in the atmosphere. The surface latent heat flux anomaly, on the other hand, does not contribute to the moistening during the initiation period (figure omitted).

To examine specific horizontal advection processes that contribute to the lower-tropospheric moistening, both the specific humidity and wind fields are decomposed into three components, the low-frequency background state (LFBS; with a period longer than 90 days), the intraseasonal (20–90-day) component, and the high-frequency (with a period less than 20 days) component. Figure 16b shows the contributions from each of nine horizontal advection terms. The largest term comes from the advection of the mean moisture by the MJO flow. The second largest term is the advection of anomalous moisture by the LFBS flow.

Figure 17a presents the horizontal patterns of the LFBS specific humidity field and the MJO wind perturbation field. Both the background specific humidity and anomalous wind fields were derived based on the time average from day –25 to –15 and vertical integration from 1000 to 700 hPa. The maximum LFBS specific humidity is located along 10°S, where the seasonal mean convection is also strongest. Note that the

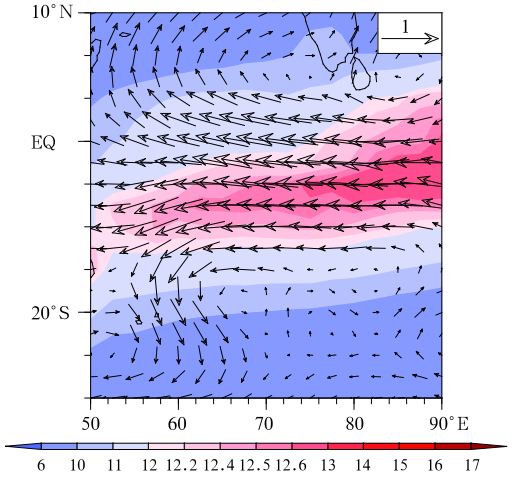

Fig. 17. Vertically integrated (1000–700 hPa) intraseasonal wind (vector; m s^{-1}) and LFBS specific humidity (shading; g kg^{-1}) fields averaged during the initiation period (day –25 to –15). From Zhao et al. (2013).

MJO flow during the initiation period is dominated by anomalous easterlies and two anticyclonic Rossby gyres over the tropical Indian Ocean. Such a wind anomaly resembles the Gill (1980) pattern and is typically observed when the suppressed MJO convection is located in the EIO. A further examination of the intraseasonal OLR field confirms that a maximum positive OLR center associated with MJO is indeed located over the EIO during the period. The anomalous winds advect the background high moisture in such a way that they increases the lower-tropospheric moisture over the initiation region (20°S–0°N, 50°–70°E).

The moisture budget analysis above reveals that the low-tropospheric moistening prior to the MJO initiation is primarily attributed to the anomalous easterly wind over the equatorial Indian Ocean. What causes the anomalous wind? There are two possible sources in generating the anomalous wind. Firstly, the anomalous easterlies may be a direct Kelvin wave response to a positive MJO heating over western Pacific (see a schematic diagram in Fig. 18a). This is possible as the preceding MJO convection travels eastward along the equator after initiated over the WIO. This represents an upstream forcing of the circumnavigating MJO mode. Secondly, the anomalous wind over the tropical Indian Ocean may be a direct Rossby wave response to a negative MJO heating over the EIO (see a schematic diagram in Fig. 18b). This is possible because a suppressed-phase MJO emerges in the WIO after a convective-phase MJO moves to the EIO; the suppressed-phase MJO then intensifies and moves eastward. This scenario represents a downstream forcing of an opposite-phase MJO in the EIO.

By examining the composite OLR and 850-hPa wind evolution maps during the initiation period, Zhao et al. (2013) noted that the anomalous easterlies over the equatorial Indian Ocean from day –25 to day –15 were primarily driven by the negative heating anomaly over the EIO, not the preceding convective MJO phase in the western equatorial Pacific. Thus the initiation of new convection over WIO is a direct Rossby wave response to the preceding suppressed MJO heating over the EIO.

To obtain the statistically robust signal of the midlatitude impact, Zhao et al. (2013) examined the upper tropospheric (200 hPa) geopotential height anomaly pattern and associated wave activity flux during the initiation period for all cases (Fig. 19). Note that the geopotential height anomaly displays a wave train pattern, with high pressure centers located southeast of South America and southeast of Africa, and low-pressure centers in between and to the east of Madagascar.

To illustrate wave energy dispersion characteristics, a phase-independent wave activity flux was calculated following Takaya and Nakamura (2001),

$$W = \frac{1}{2|\bar{u}|} \cdot \begin{pmatrix} \bar{u}(\psi_x'^2 - \psi'\psi'_{xx}) + \bar{v}(\psi'_x\psi'_y - \psi'\psi'_{xy}) \\ \bar{u}(\psi'_x\psi'_y - \psi'\psi'_{xy}) + \bar{v}(\psi_y'^2 - \psi'\psi'_{yy}) \end{pmatrix}, \quad (5)$$

where a bar and a prime denote the LFBS and the intraseasonal anomaly, W represents the horizontal wave activity flux, u and v are zonal and meridional wind velocity, and ψ denotes the streamfunction.

Figure 19 shows that there are pronounced eastward wave activity fluxes over midlatitude Southern Hemisphere, indicating that the Rossby wave energy propagates eastward. The eastward wave activity fluxes turn northward and converge onto the tropical Indian Ocean between 10° and 30°S. The wave flux convergence implies that the wave energy is accumulated over the region. A similar wave activity flux feature is also found in the lower-tropospheric geopotential height anomaly field (figure omitted), indicating that the Rossby wave train has an equivalent barotropic structure. Thus, SH midlatitude Rossby wave perturbations may trigger MJO initiation in the tropical IO through wave energy accumulation.

5.2 Idealized numerical experiments

The observational analysis above suggests that the circumnavigating signal around the globe is not critical for MJO initiation in WIO. To further support this claim, we conduct idealized numerical experiments using ECHAM4. In a control experiment, the model is integrated for 20 yr with specified climatologic monthly SST. In a sensitivity experiment

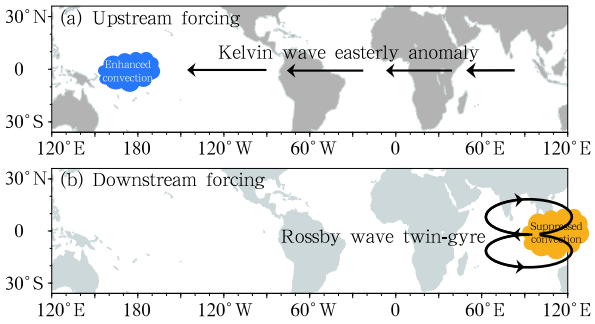

Fig. 18. Schematic diagrams illustrating (a) an upstream forcing scenario in which a positive MJO heating in the western Pacific may induce an anomalous easterly over the WIO through Kelvin wave response, and (b) a downstream forcing scenario in which a negative heating anomaly associated with suppressed-phase MJO may induce twin-gyre circulation in the tropical Indian Ocean through Rossby wave response. From Zhao et al. (2013).

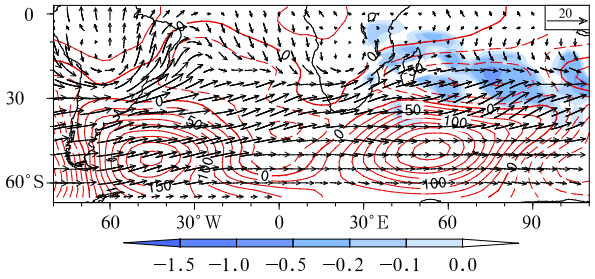

Fig. 19. 20–90-day filtered observed geopotential height anomaly (contour; $m^2\ s^{-2}$), Rossby wave activity flux (vector; $m^2\ s^{-2}$), and wave flux divergence (shading; 10^{-5} $m\ s^{-2}$; only negative values are shaded over the Indian Ocean) at 200 hPa during the initiation period from day –25 to day –15. From Zhao et al. (2013).

(named EXP_TA), the eastward-propagating intraseasonal signal is suppressed over the tropical Atlantic region (20°S–20°N, 60°W–20°E). Figure 20 shows the power spectrum of simulated intraseasonal OLR fields from both the control experiment and the EXP_TA run based on a wavenumber-frequency analysis. The magnitudes of averaged 20–90-day OLR spectrum for zonal wavenumber 1 in both experiments are quite similar. This points out that the overall eastward-propagating MJO variance has little change even though the circumnavigating mode is greatly suppressed.

The role of the midlatitude forcing effect is examined through additional sensitivity experiments. In EXP_NS, a Newtonian damping is applied over two latitudinal zones, 20°–30°S and 20°–30°N, to force the model prognostic variables toward the controlled climatologic annual cycle in the two zones. By doing so, the intraseasonal and higher-frequency variability over the zones is greatly suppressed and tropics–midlatitude connection was broken. As a result, the midlatitude influence on the tropical MJO variability was intentionally suppressed. By comparing the intraseasonal OLR spectrum in the control run and the EXP_NS run (Fig. 20c), one can see that the MJO variability in the tropics weakens significantly. For example, the averaged spectrum for zonal wavenumber 1 and 20–90-day period is reduced by 45%. Thus, the numerical result confirms that the remote forcing from midlatitudes is important in affecting the overall MJO variance in the tropics.

To further understand the relative role of the SH

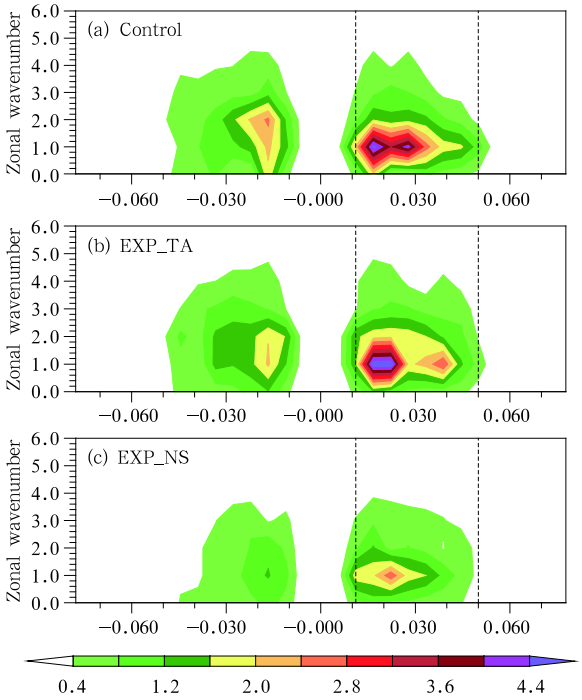

Fig. 20. Wavenumber-frequency spectra ($W^2\ m^{-4}$) of the intraseasonal OLR anomaly derived from the 20-yr simulation of the (a) Control, (b) EXP_TA, and (c) EXP_NS experiments. The spectrum analysis was done for a limited domain over 20°N–20°S, 40°E–180°.

and NH midlatitude forcing effect, we conduct other two sensitivity experiments named as "EXP_SH" and "EXP_NH". In EXP_SH (EXP_NH) run, we block the equatorward propagation of SH (NH) midlatitude waves. Compared to the control run, the averaged spectrum for zonal wavenumber 1 and 20-90-day period in the EXP_SH (EXP_NH) is reduced by 42% (7%) (figure omitted). The sensitivity experiments indicate that most of the spectrum reduction in EXP_NS is attributed to the SH wave effect. Therefore, the remote forcing from midlatitude SH is crucial for triggering MJO convection in boreal winter.

5.3 Discussion

The result presented by Zhao et al. (2013) differs from Kikuchi and Takayabu (2003; KT hereafter), who emphasized the role of circumnavigating signal in MJO initiation. Note that KT constructed the MJO signal using EOF patterns in a global tropics domain. While this methodology (and RMM method proposed by Wheeler and Hendon, 2004) can capture dominant large-scale structure and propagation characteristics, it greatly underestimates (or smoothes out) regional scale features associated with MJO convection initiation in WIO. For instance, according to KT's Fig. 5, the convection initiation appears at 60°E around t = 4. Before this initiation time, low-level wind is a pronounced westerly anomaly, which is opposite to our result (we noted significant easterly anomaly signals prior to the initiation). Secondly, total precipitable water (TPW) used in KT is a vertically-integrated variable, which is approximately in phase with the precipitation anomaly (see KT's Fig. 5); thus the TPW does not lead the convection. However, in Zhao et al. (2013), a key precursor signal is lower-tropospheric specific humidity, which leads the convection anomaly by 5–10 days.

One issue related to the MJO initiation is whether the local forcing in the tropics and the remote forcing from midlatitudes are independent. The composite study by Zhao et al. (2013) using 20-yr ERA-40 data shows that both the internal tropical process and the external midlatitude forcing process happened during the initiation period (day –25 to day –15). However, for each individual case, the two processes may occur on the same time and independently. Physical processes associated with the two processes are different. One emphasizes low-level moisture advection, and the other emphasizes upper-tropospheric Rossby wave energy accumulation. The former may trigger the convection through the gradual setup of a convectively unstable stratification, whereas the latter may trigger MJO through upper-tropospheric potential vorticity (PV) invasion.

A related issue is the cause of irregularity of MJO. The timing between MJO events is highly variable, whereas the postulated downstream tropical Rossby wave response would seem to have a more tightly bound periodicity. It is reasonable to assume that tropical forcing associated with downstream Rossby wave response is mostly responsible for successive events, while the midlatitude forcing plays a more important role in causing primary events (Matthews, 2008). It is worth mentioning that convective (or potential) instability is a necessary but not sufficient condition for convection to occur. This means that the horizontal advection of mean specific humidity by MJO flow keeps moistening the lower troposphere in the WIO until a trigger (or a lifting) either from tropics or extratropics comes along. Any scale motion may interrupt the convection initiation process through induced subsidence in the region. It is also noted that not all individual MJO events have experienced a gradual moistening before initiation. Thus, a further study is needed to identify the relative roles of the local moistening and extratropical triggering processes in each of individual MJO events.

The downstream Rossby wave forcing process proposed by Zhao et al. (2013) is somewhat similar to that of Jiang and Li (2005), who studied the MJO initiation in boreal summer. The main difference lies on the fact that the background mean flow in boreal summer is more of equatorial asymmetry, and as a result, atmospheric response to a symmetric MJO heating in the EIO is asymmetric. The initial moistening (drying) and PBL convergence (divergence) was caused by anomalous warm (cold) advection induced by anomalous cross-equatorial flow in the lower troposphere

(Jiang and Li, 2005).

Li et al. (2008) suggested that MJO initiation arose from a delayed air-sea interaction mechanism. The major processes associated with this mechanism are summarized as following. A preceding suppressed convective phase of MJO caused a warm SST anomaly due to enhanced shortwave radiation and reduced latent heat flux over the equatorial IO. The warming had a maximum center in the western IO thermocline dome and persisted after the dry-phase MJO had passed the basin. This warm SST anomaly triggered a convective phase of MJO. Thus, through this delayed air-sea interaction scenario, the preceding MJO may exert a delayed impact on the subsequent development of an opposite-phase MJO.

6. MJO interaction with high-frequency eddies

The MJO exhibits a multi-scale characteristic. Nakazawa (1988) showed that the MJO is organized by clouds with scales from individual cumulus, MCS, to SCC. The latter is often referred to as convectively coupled Kelvin waves. Within the MJO large-scale convective envelope, there are higher-frequency westward-propagating transient waves, including tropical depression (TD)-Mixed Rossby gravity wave (MRG) type perturbations (Takayabu and Nitta, 1993; Dickinson and Molinari, 2002; Aiyyer and Molinari, 2003; Frank and Roundy, 2006). As MJO propagates eastward from the Indian Ocean to the western Pacific, it interacts with higher-frequency weather systems such as TCs and lower-frequency modes such as ENSO (Liebmann et al., 1994; Maloney and Hartmann, 2000a; Vecchi and Harrison, 2002; Straub and Kiladis, 2003; Jones et al., 2004a, b; Batstone et al., 2005).

Wang and Liu (2011) constructed a scale interaction model in which there are two-way interactions between MJO and high-frequency eddies (including SCC and westward-propagating inertial-gravity waves (WIG) or two-day waves). They assumed that the westward tilted super cloud clusters are located in the west part of the convection center of the MJO, while the enhanced eastward tilted two-day waves occur to the east of the MJO convective center. Their numerical experiment showed that in such a scenario the eddy momentum transport would enhance the lower-troposphere westerly (easterly) in the rear (front) of the MJO, respectively, which presents a positive feedback for the MJO. Figure 21 illustrates a schematic diagram for such positive feedback processes.

It is worth mentioning that this scale interaction process is SCC/WIG location dependent. A negative feedback can be obtained when SCC (WIG) prevails in the front (back) of the MJO (Liu et al., 2012). The eastward tilted WIG or two-day waves also have positive eddy moisture transfer, which will moisten the middle troposphere and enhance the MJO (Liu and Wang, 2012).

To examine the two-way interaction between the tropical ISO and SSV, Zhou and Li (2010) conducted an observational analysis. A 3–10-day band-pass filter was employed to extract the synoptic-scale signal at different phases of MJO. Figure 22 shows that the

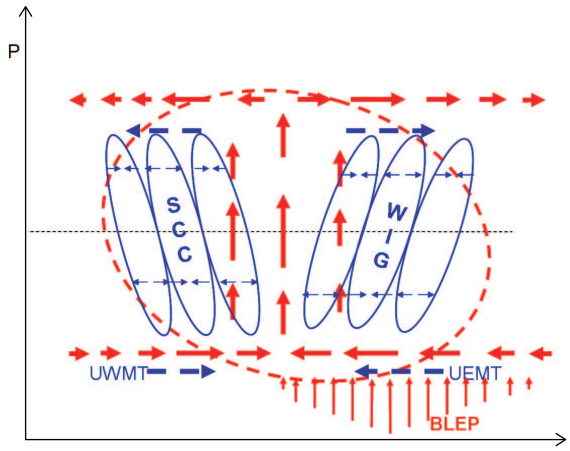

Fig. 21. Schematic diagram describing the multi-scale structure associated with MJO. The red ellipse and thick arrows represent, respectively, the convective complex and planetary-scale zonal circulations associated with MJO. The blue ellipse and thin arrows denote vertically tilted meso-synoptic disturbances (SCCs and WIG waves) and associated convergence/divergence, respectively. The thick blue arrows represent eddy-induced upscale easterly/westerly momentum transfer (UEMT/UWMT). The red thin arrows represent the boundary layer Ekman pumping (BLEP). From Wang and Liu (2011).

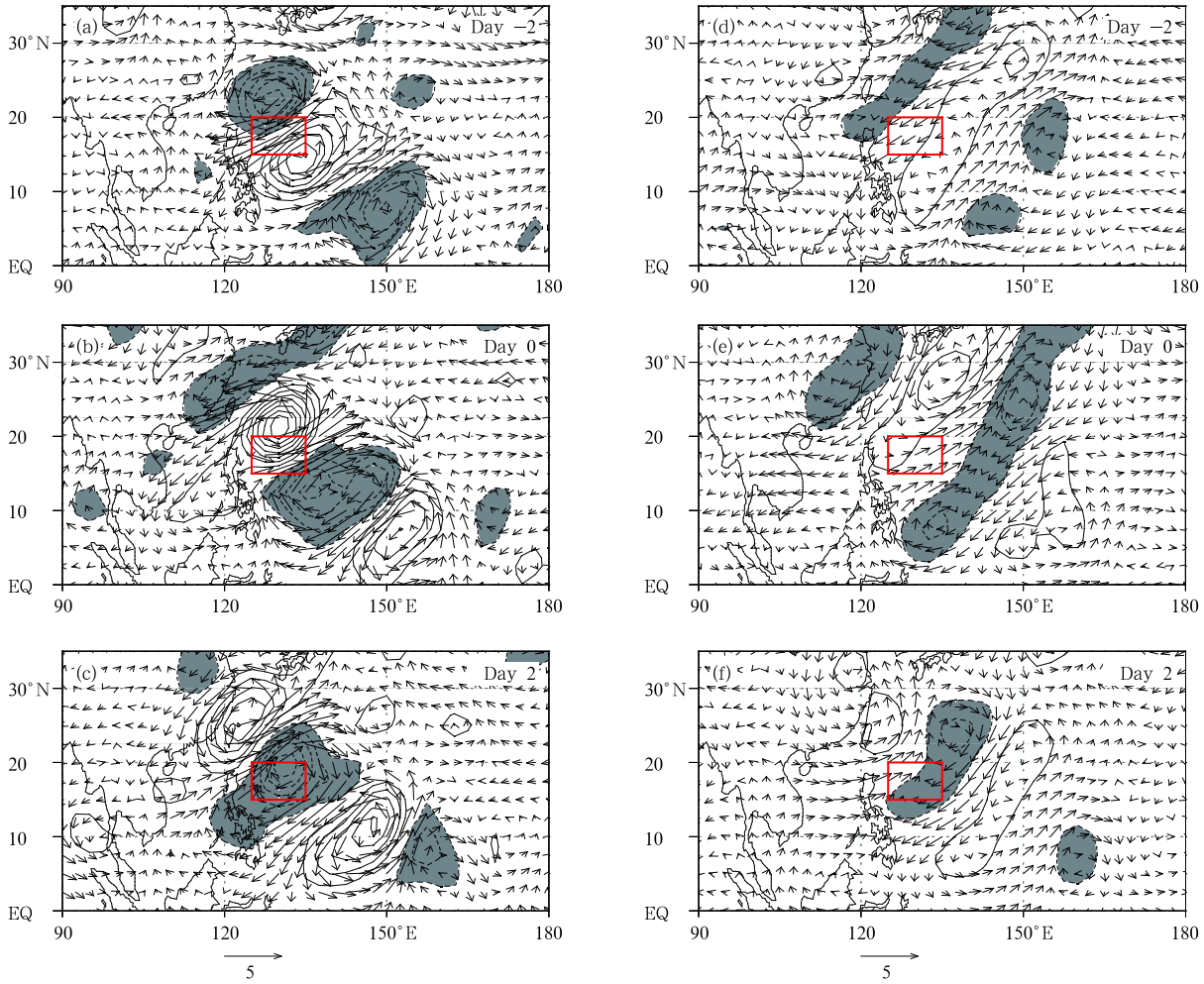

Fig. 22. Time evolution of the 3–10-day filtered QuikSCAT surface wind (vector; m s^{-1}) and vorticity (contour; interval: 0.3×10^{-5} s^{-1}) fields from day –2 to day 2 during the ISO active (a, b, c) and suppressed (d, e, f) phases. Day 0 corresponds to a time when the maximum synoptic disturbance appears in the reference (red) box. After Zhou and Li (2010).

strength of atmospheric synoptic-scale variability (SSV) differs markedly between MJO active and suppressed phases in the WNP (Zhou and Li, 2010). During the active phase, a well-organized synoptic-scale wave train with alternative cyclonic and anticyclonic flows occurs, consistent with the observed (Lau and Lau, 1990). The wave train propagates northwestward at a phase speed of about 3 m s^{-1}. In contrast, during the MJO suppressed phase, the wave train is much weaker and loosely organized.

Most of previous studies emphasized the MJO influence on SSV, and less attention was paid to the feedback of SSV to MJO. Zhou and Li (2010) examined the feedback of SSV to MJO through nonlinear rectification of surface LHF. The surface LHF may be written as:

$$\mathrm{LHF} = L\rho C_{\mathrm{E}}|\boldsymbol{V}|(q_{\mathrm{s}} - q_{\mathrm{a}}), \tag{6}$$

where $L = 2.5\times10^{6}$ J kg^{-1} is the latent heat of condensation, $\rho = 1.225$ kg m^{-3} is the air density at the standard sea level, C_{E} is an exchange coefficient, $|\boldsymbol{V}|$ is the 10-m wind speed (derived from 6-hourly ECMWF data), q_{s} is the sea surface specific humidity (derived from 6-hourly interpolated TMI SST and 6-hourly sea-level pressure from the ECMWF TOGA analysis), and q_{a} is the specific humidity at 10 m (derived from 6-hourly sea-level pressure and dew point temperature from the ECMWF TOGA analysis).

To examine to what extent SSV contributes to the intraseasonal surface LHF, zonal and meridional wind components (u, v) and air-sea humidity difference (Δq) fields are separated into three components, a low-frequency (greater than 90 days) background mean state (LFBS), a synoptic-scale component, and an intraseasonal (20–90-day) component.

Firstly, the LHF is calculated based on the sum of all the three components (which is approximately equal to the total field). The so-calculated LHF is then subject to a 20–90-day band-pass filtering. Secondly, the LHF is calculated based on the sum of the LFBS and the synoptic-scale component only (without involving the ISO component). The same 20–90-day filter is then applied to this LHF field.

By comparing the standard deviation of both the intraseasonal LHF fields, one may reveal what percentage of the intraseasonal LHF comes from the SSV-mean flow interaction. Figure 23 shows the ratio of the standard deviation of the two intraseasonal LHF fields. Note that the ratio exceeds 30% over most of the tropical Indian Ocean, western Pacific, and eastern North Pacific, indicating a great upscale feedback of SSV to the intraseasonal surface LHF in the region. Maximum SSV feedback may exceed 50% in some regions of the western and northeastern Pacific. In general, the strong upscale feedback occurs in the region where both the MJO and synoptic-scale variabilities are large.

SSV may also feed back to MJO through nonlinear rectification of atmospheric apparent heating (Hsu and Li, 2011). According to Yanai et al. (1973), the atmospheric apparent heat source (Q_1) and apparent moisture sink (Q_2) may be computed as residuals of the thermodynamic and moisture equations respectively:

$$Q_1 = c_p \frac{\partial T}{\partial t} - c_p(\omega\sigma - \boldsymbol{V}\cdot\nabla T), \tag{7a}$$

$$Q_2 = -L\frac{\partial q}{\partial t} - L\boldsymbol{V}\cdot\nabla q - L\omega\frac{\partial q}{\partial p}, \tag{7b}$$

where c_p denotes the specific heat at constant pressure, T the temperature, t the time, ω the vertical p-velocity, $\sigma = \left(\frac{RT}{c_p p}\right) - \left(\frac{\partial T}{\partial p}\right)$ the static stability, R the gas constant, p the pressure, $\boldsymbol{V}$ the horizontal velocity, ∇ the horizontal gradient operator, L the latent heat of condensation, and q the specific humidity. Q_1 represents the total diabatic heating including radiation, latent heating, surface heat flux, and sub-grid scale heat flux convergences. Q_2 represents the latent heating due to condensation or evaporation processes and sub-grid scale moisture flux convergence (Yanai et al., 1973).

The feedback of SSV to intraseasonal apparent heat and moisture sources is estimated through the following methods. Firstly, all the variables (u, v, ω, T, q) are partitioned into the LFBS, intraseasonal and synoptic-scale components. Then, Q_1 and Q_2 fields are calculated based on the sum of the LFBS, intraseasonal (10–90-day) and synoptic-scale (3–10-day) components. The so-calculated Q_1 and Q_2 fields are then subject to a 10–90-day band-pass filter to reveal the overall strength of the intraseasonal Q_1 and Q_2 variabilities. Figure 24 shows the standard deviation of 1000–100 hPa averaged 10–90-day heating rate (Q_1/c_p) calculated based on the total fields above. Note that three maximum variability centers are identified, and they are located in the Indian monsoon region (10°–20°N, 70°–100°E), the Philippine Sea-WNP sector (10°–20°N, 120°–150°E) and the tropical eastern Pacific (5°–15°N, 90°–120°W), as shown in Fig. 24a. The spatial pattern of the 10–90-day diabatic heating corresponds well to the gross features of the intraseasonal precipitation shown in Li and Wang (2005), reflecting the diabatic heating source for the

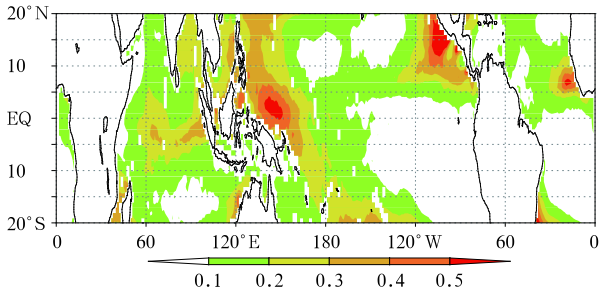

Fig. 23. Ratio of the standard deviations of the nonlinearly rectified intraseasonal latent heat flux (calculated based on synoptic-scale and LFBS fields) and the total intraseasonal latent heat flux (calculated based on synoptic-scale, MJO, and LFBS fields). From Zhou and Li (2010).

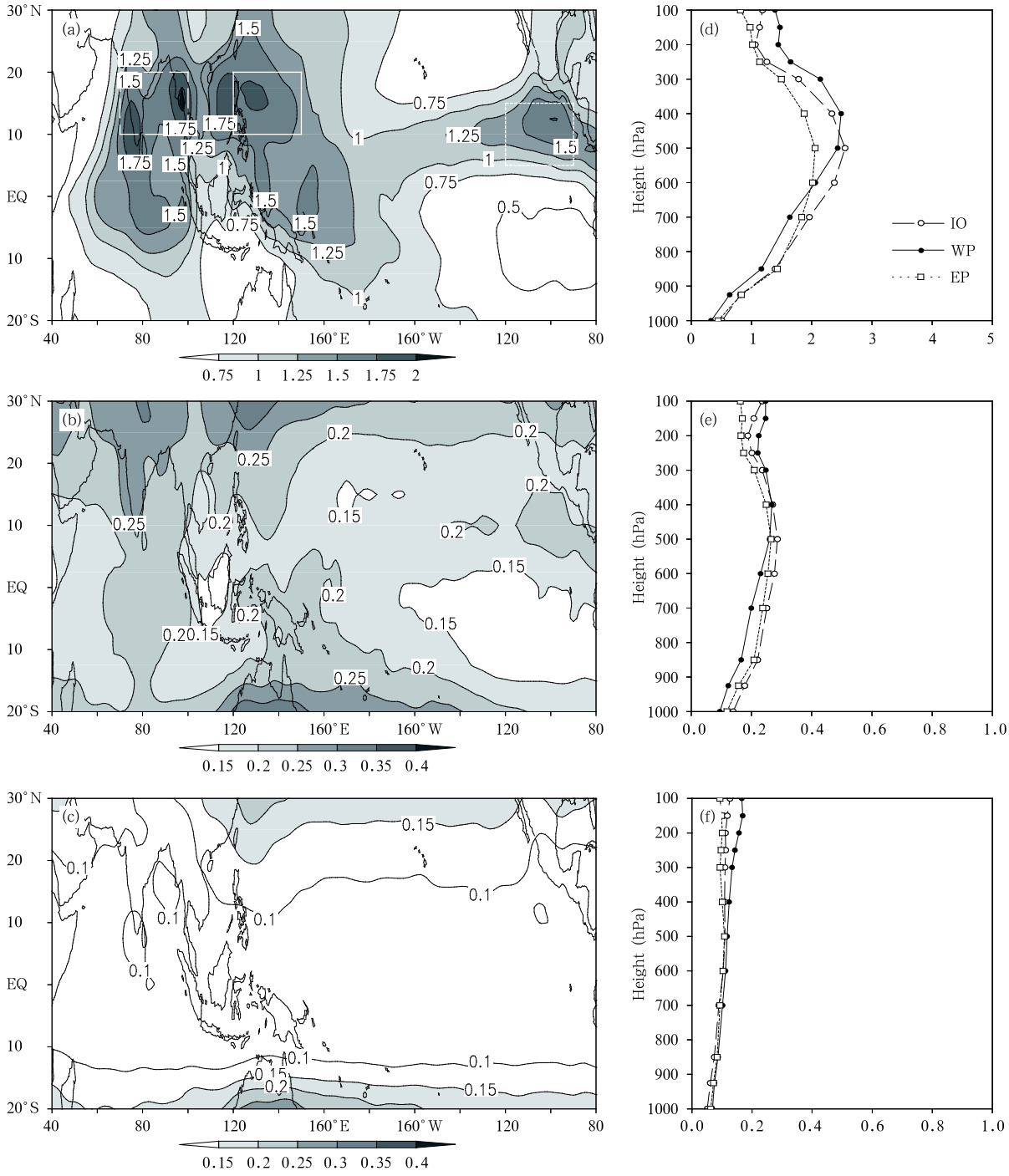

Fig. 24. Standard deviations of 10–90-day vertically averaged heating rates (Q_1/c_p; K day^{-1}) calculated based on (a) the total fields, (b) the LS components, and (c) the T-LI method (see text). Panels (d)–(f) show the vertical profiles of (a)–(c) averaged over the Indian monsoon region (10°–20°N, 70°–100°E; dashed line), the WNP sector (10°–20°N, 120°–150°E; solid line); and the tropical eastern Pacific (5°–15°N, 90°–120°W; dotted line). From Hsu and Li (2011).

summer ISO. The vertical profiles of the apparent heat sources averaged over the tropical Indian Ocean and western and eastern North Pacific show a maximum value near 400–500 hPa, with a heating rate of 2–2.5 K day^{-1} (Fig. 24d).

Secondly, the effects of eddy-eddy and eddy-mean

flow interactions on the intraseasonal apparent heat source are estimated. Two methods are developed for this purpose. One is to calculate the Q_1 and Q_2 fields based on the sum of the LFBS and synoptic (hereafter LS) components (without involving the MJO flow). The so-calculated Q_1 and Q_2 fields are then subject to a 10–90-day band-pass filter. This calculation, however, does not include the effect of the eddy-MJO interaction. The standard deviation of vertically averaged 10–90-day heating rate (Q_1/c_p) calculated based on the LS components is displayed in Fig. 24b. The amplitude of the nonlinearly rectified heating over the tropical Indian Ocean and western Pacific regions is 0.2–0.25 K day^{-1} (Fig. 24b). The vertical profiles of the nonlinearly rectified heating fields averaged over the three active ISO regions show a maximum in the mid troposphere (Fig. 24e).

The second method has the following procedure: 1) calculating Q_1 and Q_2 with the sum of the LFBS and ISO (hereafter LI) components, 2) applying a 10–90-day band-pass filter to the resulting Q_1 and Q_2 fields, 3) subtracting the time series of the Q_1 and Q_2 fields above from the time series of the Q_1 and Q_2 fields calculated based on the total components. The so-calculated intraseasonal Q_1 and Q_2 fields reflect the interactions of SSV with both the LFBS and ISO flows. The second method is called the T-LI method.

The amplitude of the nonlinearly rectified Q_1 field derived by the T-LI method is a little weaker (Fig. 24c), compared with that derived based on the LS components (Fig. 24b), even though their spatial distributions are similar. The same methods are applied to the Q_2 field. The overall horizontal patterns of the calculated intraseasonal Q_2 fields (figure omitted) are quite similar to the corresponding Q_1 fields. The major difference lies in the vertical profiles. The maximum amplitudes of the total and nonlinearly rectified intraseasonal Q_2 fields all appear in the lower troposphere (between 700 and 850 hPa).

Figure 25 shows the ratios of standard deviations of the nonlinearly rectified Q_1 and Q_2 fields calculated based on the two methods to standard deviations of the total intraseasonal Q_1 and Q_2 fields. The nonlinearly rectified Q_1 and Q_2 based on both the methods

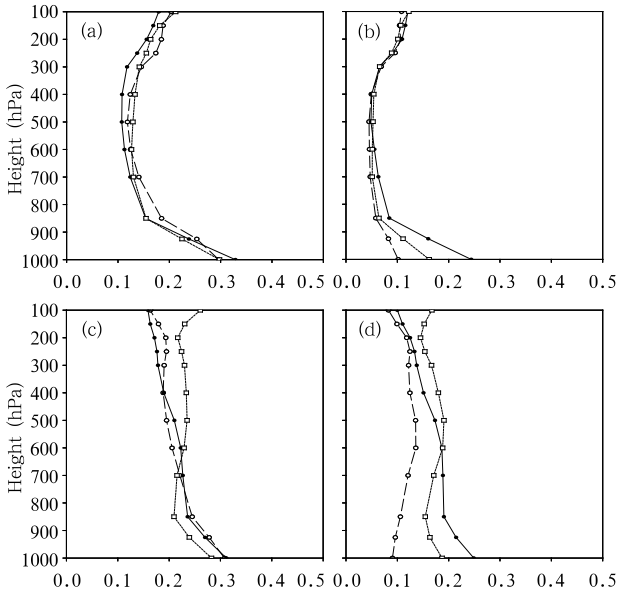

Fig. 25. Vertical distributions of ratios of standard deviations of the nonlinear rectified 10–90-day Q_1 field calculated based on the (a) LS components and (b) T-LI method vs the standard deviations of the total intraseasonal Q_1 over the three box regions shown in Fig. 24a. (c, d) As (a, b), but for Q_2. From Hsu and Li (2011).

account for 10%–30% of the total intraseasonal Q_1 and Q_2 variabilities, indicating that high-frequency eddies can significantly modulate the intraseasonal diabatic heating in the active MJO and SSV regions.

The role of scale interactions in the maintenance of eddy kinetic energy (EKE) during the MJO wet and dry phases was examined through the construction of a new eddy energetic diagnostic tool that separates the effect of MJO and LFBS (Hsu et al., 2011). As the summer LFBS always contributes positively toward the EKE, the synoptic eddies extract energy from MJO during its active phase. This positive barotropic energy conversion occurs when the synoptic eddies interact with low-level cyclonic and convergent MJO flows. This contrasts to the MJO dry phase during which the synoptic eddies lose kinetic energy to the MJO flow. The anticyclonic and divergent MJO flow during the dry phase is responsible for the negative barotropic energy conversion.

In addition, SSV may exert an upscale feedback to MJO through eddy momentum transport (Majda

and Stechmann, 2009; Hsu and Li, 2011) and the modulation of intraseasonal SST variations (Li et al., 2008).

7. Summary and discussion

In this review paper, some of the recent progress in understanding MJO dynamics is described, including mechanisms for MJO eastward propagation, planetary-scale selection, seasonality, initiation, and multi-scale interaction.

The moisture dynamics responsible for the eastward propagation of MJO were examined through a moisture budget diagnosis based on the ERA-40 reanalysis during DJF of 1979–2001 (Hsu and Li, 2012). A positive moisture anomaly appears at the PBL (1000–700 hPa) to the east of MJO convection. This east-west moisture asymmetry leads to a convectively unstable stratification in the lower troposphere and triggers shallow convection. The shallow convection further transports water vapor upward, leading to the onset of deep convection. This stepwise development of MJO shallow-to-deep convection agrees well with previous studies (e.g., Kemball-Cook and Weare, 2001; Kikuchi and Takayabu, 2004; Benedict and Randall, 2007). Therefore, a key element for MJO eastward propagation is its zonal moisture asymmetry.

A moisture budget analysis was performed to understand the cause of the moisture asymmetry (Hsu and Li, 2012). The diagnosis result indicated that the vertical advection of mean moisture by anomalous ascending motion associated with PBL convergence dominated the low-level moistening ahead of MJO convection. A diagnosis of the PBL momentum budget further showed that the contribution to the PBL convergence by the heating-induced free-atmospheric wave dynamics was dominant and it accounted for 75%–90% of the total boundary layer convergence. The contribution by anomalous SST due to SST-gradient-induced pressure gradient (Lindzen and Nigam, 1987) accounted for 10%–25% of the total boundary layer convergence. The result suggests that both the internal atmospheric dynamics and air-sea interactions contribute to the PBL convergence and the moisture asymmetry and thus are responsible for the eastward propagation of MJO.

The cause of the planetary scale selection of the MJO was investigated through a 2.5-layer atmospheric model (Li and Zhou, 2009). Initially, a Kelvin wave perturbation with zonal wavenumbers 1–15 was specified respectively. In the presence of a frictional boundary layer, the most unstable mode prefers a short wavelength under a linear heating; but with a nonlinear heating, the zonal wavenumber-one grows fastest. Thus the numerical simulations point out the crucial importance of the nonlinear heating in the MJO planetary scale selection.

The cause of this scale selection under the nonlinear heating is attributed to the distinctive phase speeds between the dry Kelvin wave and the wet Kelvin-Rossby wave couplet. The faster dry Kelvin wave triggered by a convective branch may "catch up" and suppress another convective branch, which travels at the phase speed of the wet Kelvin-Rossby wave couplet, ahead of it, if the distance between the two neighboring convective branches is smaller than a critical distance (about 16000 km). The interference between the dry Kelvin wave and the wet Kelvin-Rossby wave couplet eventually dissipates and "filters out" shorter wavelength perturbations, leading to a longwave selection.

The distinctive MJO propagation feature between boreal winter and summer was investigated through an eigenvalue analysis. It was found that atmospheric moist Kelvin waves are unstable while Rossby waves are stable in boreal winter when maximum mean ascending motion and moisture are near the equator; atmospheric moist Kelvin waves stabilize while Rossby waves become unstable in boreal summer, when maximum mean ascending motion and moisture are more than one Rossby radius of deformation away from the equator. The theoretical study suggests that the marked northward shift of the thermal equator in boreal summer is an essential cause of meridional bifurcation of the MJO convection off Sumatra.

The precursor signals of MJO convection initiation in boreal winter were investigated through the diagnosis of 20-yr ERA-40 reanalysis data (Zhao et

al., 2013). The western equatorial Indian Ocean is a key region of the MJO initiation. A marked increase of low-level specific humidity appeared 5–10 days prior to the convection initiation. The increased moisture caused convective instability, leading to the onset of the convection.

A diagnosis of lower-tropospheric moisture budgets showed that the moisture increase was caused primarily by the horizontal advection of the mean specific humidity by anomalous flows induced due to downstream Rossby wave response to a preceding suppressed-phase MJO over the eastern Indian Ocean.

The midlatitude wave activity flux prior to the MJO initiation was diagnosed (Zhao et al., 2013). It was found that SH midlatitude Rossby waves contributed to MJO initiation over the western Indian Ocean through wave energy accumulation. Idealized numerical experiments confirmed the importance of SH midlatitude wave perturbations in affecting the MJO variance in the tropics.

Two-way interactions between the MJO and high-frequency motion were investigated. By constructing a theoretical model, Wang and Liu (2011) showed that convectively coupled Kelvin waves and westward-propagating inertial-gravity waves could feed positively back to MJO flow through eddy momentum transport, provided that the higher-frequency Kelvin waves (inertial-gravity waves) were placed to the west (east) of the MJO convective center. Through the analysis of observational data, Zhou and Li (2010) showed that MJO significantly modulated the synoptic-scale variability. For example, synoptic wave trains in WNP were stronger (weaker) during the MJO active (suppressed) phase. The synoptic-scale motion can exert an upscale feedback to MJO through the nonlinear rectification of the surface latent heat flux, atmospheric apparent heat source (Q_1) and moisture sink (Q_2), and eddy momentum transport (Zhou and Li, 2010; Hsu and Li, 2011). The nonlinearly rectified LHF and diabatic heating due to eddy-mean flow interactions account for 30%–50% and 10%–30%, respectively, of their total intraseasonal variabilities in the WNP.

Over the past decades, the improvements of numerical weather forecast model physics, data assimilation methodology and computing technology have significantly advanced 3–7-day medium range weather forecasts (Saha et al., 2006). Climate prediction has also shown capability in seasonal range (Wang et al., 2009). However, the extended range (10–30 days) forecast has so far received less attention and is considered as a forecast gap between short-range weather and long-term climate predictions (Shukla et al., 2010). How to improve the extended range forecast of high-impact events remains a challenge in both weather and climate services.

The major predictability source at extended range lies in the atmospheric MJO. Numerous studies have indentified the modulations of the MJO on monsoon activity and the occurrence of heavy monsoon rainfall (e.g., Yasunari, 1979; Lau and Chan, 1986). The ISO regulates the genesis, frequency, track, and strength of tropical cyclones (e.g., Liebmann et al., 1994; Maloney and Hartmann, 2000a, b). Hence the MJO has significant impacts on the skill of medium-to-extended range weather forecasts (Hendon et al., 2000; Jones et al., 2000). In Southeast China, extreme floods occurring in pre-monsoon and summer monsoon seasons were often associated with the MJO activities (Zhu et al., 2003; Yang and Li, 2003; Mao and Wu, 2006; Mao et al., 2010; Yang et al., 2010). Significant northward-propagating 30–60-day ISO from the tropics was observed in the 1998 Yangtze River flooding event (Zhu et al., 2003). Thus, the connection between the MJO activities and heavy rainfall events provides predictability sources for predicting low-frequency precipitation events at 10–30-day leads.

One way to achieve extended-range forecast is to rely on dynamic models. Most of current operational models, however, have low skills in predicting the MJO (Kim et al., 2009). Another way is to reply on empirical model (e.g., Lo and Hendon, 2000; Jones et al., 2004a; Jiang et al., 2008). Most of these statistical models are based on the empirical orthogonal function (EOF) analysis or the regression method. Different from the above approach, we proposed a spatial-temporal projection model (STPM). The special feature of this new model is the use of extended

singularity value decomposition (E-SVD) technique. In other words, the model utilizes the spatial and temporal information of predictor-predictand coupled patterns. A preliminary application of this method to 10–30-day forecast of rainfall over South China for 2008–2012 indicates that the ensemble prediction of the STPM achieves a useful skill (with a temporal correlation coefficient exceeding the 95% confidence level) up to a 30-day lead. Currently we are applying this methodology to other parts of China and to the global tropics.

Acknowledgments. Contributions by Drs. Pangchi Hsu, Xianan Jiang, Fei Liu, Chongbo Zhao, Chunhua Zhou, Jianyun Gao, and Dejun Gu are greatly appreciated.

REFERENCES

Aiyyer, A. R., and J. Molinari, 2003: Evolution of mixed Rossby-gravity waves in idealized MJO environments. *J. Atmos. Sci.*, **60**(23), 2837–2855.

Annamalai, H., J. M. Slingo, K. R. Sperber, et al., 1999: The mean evolution and variability of the Asian summer monsoon: Comparison of ECMWF and NCEP-NCAR reanalyses. *Mon. Wea. Rev.*, **127**(6), 1157–1186.

——, and ——, 2001: Active/break cycles: Diagnosis of the intraseasonal variability of the Asian summer monsoon. *Climate Dyn.*, **18**(1–2), 85–102.

Batstone, C. P., A. J. Matthews, and D. P. Stevens, 2005: Coupled ocean-atmosphere interactions between the Madden-Julian oscillation and synoptic-scale variability over the warm pool. *J. Climate*, **18**(12), 2004–2020.

Benedict, J., and D. A. Randall, 2007: Observed characteristics of the MJO relative to maximum rainfall. *J. Atmos. Sci.*, **64**(7), 2332–2354.

Biello, J. A., and A. J. Majda, 2005: A new multi-scale model for the Madden-Julian oscillation. *J. Atmos. Sci.*, **62**(6), 1694–1721.

——, ——, and M. W. Moncrieff, 2007: Meridional momentum flux and super-rotation in the multi-scale IPESD MJO model. *J. Atmos. Sci.*, **64**(5), 1636–1651.

Chang, C. P., 1977: Viscous internal gravity waves and low-frequency oscillations in the tropics. *J. Atmos. Sci.*, **34**(6), 901–910.

——, and H. Lim, 1988: Kelvin-wave CISK: A possible mechanism for the 30–50-day oscillation. *J. Atmos. Sci.*, **45**(11), 1709–1720.

Chao, W. C., and B. Chen, 1999: On the role of surface friction in tropical intraseasonal oscillation. Preprints, 23-d Conf. on Hurricanes and Tropical Meteorology, Vol. II, Dallas, TX, Amer. Meteor. Soc., 815–818.

Chen, T.-C. and M. Murakami, 1988: The 30–50-day variation of convective activity over the western Pacific Ocean with the emphasis on the northwestern region. *Mon. Wea. Rev.*, **116**(4), 892–906.

——, R. Y. Tzeng, and M. C. Yen, 1988: Development and life cycle of the Indian monsoon: Effect of the 30–50-day oscillation. *Mon. Wea. Rev.*, **116**(11), 2183–2199.

Dickinson, M., and J. Molinari, 2002: Mixed Rossby-gravity waves and western Pacific tropical cyclogenesis. Part I: Synoptic evolution. *J. Atmos. Sci.*, **59**(14), 2183–2195.

Ding, Q. H., and B. Wang, 2007: Intraseasonal teleconnection between the summer Eurasian wave train and the Indian monsoon. *J. Climate*, **20**(15), 3751–3767.

Ding, Y. H., 2007: The variability of the Asian summer monsoon. *J. Meteor. Soc. Japan*, **85B**, 21–54.

Emanuel, K. A., 1987: An air-sea interaction model of intraseasonal oscillations in the tropics. *J. Atmos. Sci.*, **44**(16), 2324–2340.

——, 1994: *Atmospheric Convection*. Oxford Univ. Press, New York, 580 pp.

Flatau, M. K., P. Flatau, P. Phoebus, et al., 1997: The feedback between equatorial convection and local radiative and evaporative processes: The implications for intraseasonal oscillations. *J. Atmos. Sci.*, **54**(19), 2373–2386.

Frank, W. M., and P. E. Roundy, 2006: The role of tropical waves in tropical cyclogenesis. *Mon. Wea. Rev.*, **134**(9), 2397–2417.

Fu, X., B. Wang, T. Li, et al., 2003: Coupling between northward propagating ISO and SST in the Indian Ocean. *J. Atmos. Sci.*, **60**, 1733–1753.

Gadgil, S., and J. Srinivasan, 1990: Low frequency variation of tropical convergence zones. *Meteor. Atmos. Phys.*, **44**(1–4), 119–132.

Gautier, C., and B. DiJuli, 1990: Cloud effect on air-sea interactions during the 1979 Indian summer monsoon as studied from satellite observations. *Meteor. Atmos. Phys.*, **44**, 119–132.

Gill, A. E., 1980: Some simple solutions for heat-induced tropical circulation. *Quart. J. Roy. Meteor. Soc.*, **106**(449), 447–462.

Goswami, B. N., 1998: Interannual variations of Indian summer monsoon in a GCM: External conditions versus internal feedback. *J. Climate*, **11**(4), 501–522.

Goswami, P., and R. K. Rao, 1994: A dynamical mechanism for selective excitation of the Kelvin mode at timescale of 30–50 days. *J. Atmos. Sci.*, **51**(19), 2769–2779.

Grabowski, W. W., 2001: Coupling cloud processes with the large-scale dynamics using the cloud-resolving convection parameterization (CRCP). *J. Atmos. Sci.*, **58**(9), 978–997.

Hartmann, D. L., and M. L. Michelsen, 1989: Intraseasonal periodicities in Indian rainfall. *J. Atmos. Sci.*, **46**(18), 2838–2862.

——, and E. D. Maloney, 2001: The Madden-Julian oscillation, barotropic dynamics, and North Pacific tropical cyclone formation. Part II: Stochastic barotropic modeling. *J. Atmos. Sci.*, **58**(17), 2559–2570.

——, M. L. Michelsen, and S. A. Kelein, 1992: Seasonal variations of tropical intraseasonal oscillations: A 20–25-day oscillation in the western Pacific. *J. Atmos. Sci.*, **49**(14), 1277–1289.

Hendon, H. H., and B. Liebmann, 1994: Organization of convection within the Madden-Julian oscillation. *J. Geophys. Res.*, **99**(D4), 8073–8083.

——, and M. L. Salby, 1994: The life cycle of Madden-Julian oscillation. *J. Atmos. Sci.*, **51**, 2207–2219.

——, and J. Glick, 1997: Intraseasonal air-sea interaction in the tropical Indian and Pacific oceans. *J. Climate*, **10**(4), 647–661.

——, B. Liebmann, M. Newman, et al., 2000: Medium-range forecast errors associated with active episodes of the Madden-Julian oscillation. *Mon. Wea. Rev.*, **128**(1), 69–86.

Holton, J. R., 1992: *An Introduction to Dynamic Meteorology (Third Edition)*. Academic Press, San Diego, 511 pp.

Houze, R. A., Jr., 1993: *Cloud Dynamics*. Academic Press, San Diego, 573 pp.

Hsu, H. -H., and C.-H. Weng, 2001: Northwestward propagation of the intraseasonal oscillation in the western North Pacific during the boreal summer: Structure and mechanism. *J. Climate*, **14**(18), 3834–3850.

——, and M. Lee, 2005: Topographic effects on the eastward propagation and initiation of the Madden-Julian oscillation. *J. Climate*, **18**(6), 795–809.

——, B. J. Hoskins, and F.-F. Jin, 1990: The 1985/86 intraseasonal oscillation and the role of the extratropics. *J. Atmos. Sci.*, **47**(7), 823–839.

Hsu, P.-C., and T. Li, 2011: Interactions between boreal summer intraseasonal oscillations and synoptic-scale disturbances over the western North Pacific. Part II: Apparent heat and moisture sources and eddy momentum transport. *J. Climate*, **24**(3), 942–961.

——, and ——, 2012: Role of the boundary layer moisture asymmetry in causing the eastward propagation of the Madden-Julian oscillation. *J. Climate*, **25**(14), 4914–4931.

——, ——, and C.-H. Tsou, 2011: Interactions between boreal summer intraseasonal oscillations and synoptic-scale disturbances over the western North Pacific. Part I: Energetics diagnosis. *J. Climate*, **24**(3), 927–941.

Jiang, X., and T. Li, 2005: Re-initiation of the boreal summer intraseasonal oscillation in the tropical Indian Ocean. *J. Climate*, **18**(18), 3777–3795.

——, ——, and B. Wang, 2004: Structures and mechanisms of the northward propagating boreal summer intraseasonal oscillation. *J. Climate*, **17**(5), 1022–1039.

——, D. E. Waliser, M. C. Wheeler, et al., 2008: Assessing the skill of an all-season statistical forecast model for the Madden-Julian oscillation. *Mon. Wea. Rev.*, **136**(6), 1940–1956.

Jones, C., and B. C. Weare, 1996: The role of low-level moisture convergence and ocean latent heat fluxes in the Madden and Julian oscillation: An observational analysis using ISCCB data and ECMWF analyses. *J. Climate*, **9**, 3086–3104.

——, D. E. Waliser, J.-K. E. Schemm, et al., 2000: Prediction skill of the Madden and Julian oscillation in dynamical extended range forecasts. *Climate Dyn.*, **16**(4), 273–289.

——, D. E. Waliser, K. M. Lau, et al., 2004a: The Madden-Julian oscillation and its impact on Northern Hemisphere weather predictability. *Mon. Wea. Rev.*, **132**(6), 1462–1471.

——, ——, ——, et al., 2004b: Global occurrences of extreme precipitation and the Madden-Julian oscillation: Observations and predictability, *J. Climate*, **17**(23), 4575–4589.

——, L. M. V. Carvalho, W. Higgins, et al., 2004c: Climatology of tropical intraseasonal convective anomalies: 1979–2002. *J. Climate*, **17**(3), 523–539.

Johnson, R. H., T. M. Rickenbach, S. A. Rutledge, et al., 1999: Trimodal characteristics of tropical convection. *J. Climate*, **12**(8), 2397–2418.

Kawamura, R., T. Murakami, and B. Wang, 1996: Tropical and midlatitude 45-day perturbations over the western Pacific during the northern summer. *J. Meteor. Soc. Japan*, **74**(6), 867–890.

Kemball-Cook, S. R., and B. Wang, 2001: Equatorial waves and air-sea interaction in the boreal summer intraseasonal oscillation. *J. Climate*, **14**(13), 2923–2942.

——, and B. C. Weare, 2001: The onset of convection in the Madden-Julian oscillation. *J. Climate*, **14**(5), 780–793.

Khouider, B., and A. J. Majda, 2006: A simple multicloud parameterization for convectively coupled tropical waves. Part I: Linear analysis. *J. Atmos. Sci.*, **63**(4), 1308–1323.

Kikuchi, K., and Y. N. Takayabu, 2003: Equatorial circumnavigation of moisture signal associated with the Madden-Julian oscillation (MJO) during boreal winter. *J. Meteor. Soc. Japan*, **81**(4), 851–869.

——, and ——, 2004: The development of organized convection associated with the MJO during TOGA COARE IOP: Trimodal characteristics. *Geophys. Res. Lett.*, **31**, L10101.

Kiladis, G. N., K. H. Straub, and P. T. Haertel, 2005: Zonal and vertical structure of the Madden-Julian oscillation. *J. Atmos. Sci.*, **62**(8), 2790–2809.

Kim, D., K. W. Sperber, D. Stern, et al., 2009: Application of MJO simulation diagnostics to climate models. *J. Climate*, **22**(23), 6413–6436.

Knutson, T. R., and K. M. Weickmann, 1987: 30–60 day atmospheric oscillations: Composite life cycles of convection and circulation anomalies. *Mon. Wea. Rev.*, **115**(7), 1407–1436.

Krishnamurti, T. N., 1985: Summer monsoon experiment—A review. *Mon. Wea. Rev.*, **113**(9), 1590–1626.

——, and D. Subrahmanyam, 1982: The 30–50-day mode at 850 mb during MONEX. *J. Atmos. Sci.*, **39**(9), 2088–2095.

——, D. R. Chakraborty, N. Cubukcu, et al., 2003: A mechanism of the MJO based on interactions in the frequency domain. *Quart. J. Roy. Meteor. Soc.*, **129**(593), 2559–2590.

Lau, N.-C., and K.-M. Lau, 1986: The structure and propagation of intraseasonal oscillation appearing in a GFDL general circulation model. *J. Atmos. Sci.*, **43**(19), 2023–2047.

Lau, K.-H., and N.-C. Lau, 1990: Observed structure and propagation characteristics of tropical summertime synoptic-scale disturbances. *Mon. Wea. Rev.*, **118**(9), 1888–1993.

Lau, K.-M., and P. H. Chan, 1986: Aspects of the 40–50-day oscillation during the northern summer as inferred from outgoing longwave radiation. *Mon. Wea. Rev.*, **114**(7), 1354–1367.

——, and L. Peng, 1987: Origin of low frequency (intraseasonal) oscillation in the tropical atmosphere. Part I: The basic theory. *J. Atmos. Sci.*, **44**(6), 950–972.

——, and C.-H. Sui, 1997: Mechanisms of short-term sea surface temperature regulation: Observations during TOGA-COARE. *J. Climate*, **10**(3), 465–472.

——, and D. E. Waliser, 2005: *Intraseasonal Variability of the Atmosphere-Ocean Climate System*. Springer, Heidelberg, Germany, 474 pp.

Lawrence, D. M., and P. J. Webster, 2002: The boreal summer intraseasonal oscillation: Relationship between northward and eastward movement of convection. *J. Atmos. Sci.*, **59**(9), 1593–1606.

Li Chongyin and Liao Qinghai, 1996: Behavior of coupled modes in a simple nonlinear air-sea interaction model. *Adv. Atmos. Sci.*, **13**(2), 183–195.

——, Cho Han-Ru, and Wang Jough-Tai, 2002: CISK Kelvin wave with evaporation-wind feedback and air-sea interaction—A further study of tropical intraseasonal oscillation mechanism. *Adv. Atmos. Sci.*, **19**(3), 379–389.

Li, T., and B. Wang, 1994a: The influence of sea surface temperature on the tropical intraseasonal oscillation: A numerical study. *Mon. Wea. Rev.*, **122**(10), 2349–2362.

——, and ——, 1994b: A thermodynamic equilibrium climate model for monthly mean surface winds and precipitation over the tropical Pacific. *J. Atmos. Sci.*, **51**(11), 1372–1385.

——, and ——, 2005: A review on the western North Pacific monsoon: Synoptic-to-interannual variabilities. *Terrestrial, Atmospheric and Oceanic Sciences*, **16**(2), 285–314.

——, and C. Zhou, 2009: Planetary scale selection of the Madden-Julian oscillation. *J. Atmos. Sci.*, **66**(8), 2429–2443.

——, F. Tam, X. H. Fu, et al., 2008: Causes of the intraseasonal SST variability in the tropical Indian Ocean. *Atmosphere-Ocean Science Letters*, **1**, 18–23.

Liebmann, B., H. H. Hendon, and J. D. Glick, 1994: The relationship between tropical cyclones of the western Pacific and Indian oceans and the Madden-Julian oscillation. *J. Meteor. Soc. Japan*, **72**, 401–412.

Lin, A.-L., T. Li, X. H. Fu, et al., 2011: Effects of air-sea coupling on the boreal summer intraseasonal oscillations over the tropical Indian Ocean. *Climate Dyn.*, **37**(11–12), 2303–2322.

Lin, J.-L., G. N. Kiladis, B. E. Mapes, et al., 2006: Tropical intraseasonal variability in 14 IPCC AR4 climate models. Part I: Convective signals. *J. Climate*, **19**(12), 2665–2690.

Lindzen, R. S., and S. Nigam, 1987: On the role of sea surface temperature gradients in forcing low-level winds and convergence in the tropics. *J. Atmos. Sci.*, **44**(17), 2418–2436.

Liu, F., and B. Wang, 2012: A model for the interaction between the 2-day waves and moist Kelvin waves. *J. Atmos. Sci.*, **69**(2), 611–625.

——, G. Huang, and L. C. Feng, 2012: Critical roles of convective momentum transfer in sustaining the multi-scale Madden-Julian oscillation. *Theor. Appl. Climatol.*, **108**(3–4), 471–477.

Lo, F., and H. H. Hendon, 2000: Empirical extended-range prediction of the Madden-Julian oscillation. *Mon. Wea. Rev.*, **128**(7), 2528–2543.

Madden, R. A., and P. R. Julian, 1971: Detection of a 40–50 day oscillation in the zonal wind in the tropical Pacific. *J. Atmos. Sci.*, **28**(5), 702–708.

——, and ——, 1972: Description of global-scale circulation cells in the tropics with a 40–50-day period. *J. Atmos. Sci.*, **29**(6), 3138–3158.

——, 1986: Seasonal variations of the 40–50-day oscillation in the tropics. *J. Atmos. Sci.*, **43**(24), 3138–3158.

——, and P. R. Julian, 1994: Observations of the 40–50-day tropical oscillation—A review. *Mon. Wea. Rev.*, **122**(5), 814–837.

Majda, A. J., and J. A. Biello, 2004: A multiscale model for tropical intraseasonal oscillations. *Proc. Natl. Acad. Sci.*, **101**(14), 4736–4741.

——, and S. N. Stechmann, 2009: A simple dynamical model with features of convective momentum transport. *J. Atmos. Sci.*, **66**(2), 373–392.

Maloney, E. D., 2009: The moist static energy budget of a composite tropical intraseasonal oscillation in a climate model. *J. Climate*, **22**(3), 711–729.

——, and D. L. Hartmann, 1998: Frictional moisture convergence in a composite life cycle of the Madden-Julian oscillation. *J. Climate*, **11**, 2387–2403.

——, and ——, 2000a: Modulation of eastern North Pacific hurricanes by the Madden-Julian oscillation. *J. Climate*, **13**(9), 1451–1460.

——, and ——, 2000b: Modulation of hurricane activity in the Gulf of Mexico by the Madden-Julian oscillation. *Science*, **287**(5460), 2002–2004.

——, and ——, 2001: The Madden-Julian oscillation, barotropic dynamics, and North Pacific tropical cyclone formation. Part I: Observations. *J. Atmos. Sci.*, **58**, 2545–2558.

——, and M. J. Dickinson, 2003: The intraseasonal oscillation and the energetics of summertime tropical western North Pacific synoptic-scale disturbances. *J. Atmos. Sci.*, **60**(17), 2153–2168.

——, and A. H. Sobel, 2004: Surface fluxes and ocean coupling in the tropical intraseasonal oscillation. *J. Climate*, **17**(22), 4368–4386.

Mao, J. Y., and G.-X. Wu, 2006: Intraseasonal variations of the Yangtze rainfall and its related atmospheric circulation features during the 1991 summer. *Climate Dyn.*, **27**(7–8), 815–830.

——, Z. Sun, and G.-X. Wu, 2010: 20–50-day oscillation of summer Yangtze rainfall in response to intraseasonal variations in the subtropical high over the western North Pacific and South China Sea. *Climate Dyn.*, **34**, 747–761.

Matthews, A. J., 2000: Propagation mechanism for the Madden-Julian oscillation. *Quart. Roy. Meteor. Soc.*, **126**(569), 2637–2651.

——, 2008: Primary and successive events in the Madden-Julian oscillation. *Quart. J. Roy. Meteor. Soc.*, **134**(631), 439–453.

Mo, K. C., 2000: Intraseasonal modulation of summer precipitation over North America. *Mon. Wea. Rev.*, **128**(5), 1490–1505.

Moncrieff, M. W., 2004: Analytic representation of the large-scale organization of tropical convection. *J. Atmos. Sci.*, **61**, 1521–1538.

Moskowitz, B. M., and C. S. Bretherton, 2000: An analysis of frictional feedback on a moist equatorial Kelvin mode. *J. Atmos. Sci.*, **57**(13), 2188–2206.

Murakami, T., 1980: Empirical orthogonal function analysis of satellite-observed outgoing longwave radiation during summer. *Mon. Wea. Rev.*, **108**(2), 205–222.

——, and T. Nakazawa, 1985: Tropical 45-day oscillations during the 1979 Northern Hemisphere summer. *J. Atmos. Sci.*, **42**(11), 1107–1122.

Myers, D., and D. E. Waliser, 2003: Three-dimensional water vapor and cloud variations associated with the Madden-Julian oscillation during Northern Hemisphere winter. *J. Climate*, **16**, 929–950.

Nakazawa, T., 1988: Tropical super clusters within intraseasonal variations over the western Pacific. *J. Meteor. Soc. Japan*, **66**, 823–839.

Neelin, J. D., I. M. Held, and K. H. Cook, 1987: Evaporation-wind feedback and low-frequency variability in the tropical atmosphere. *J. Atmos. Sci.*, **44**(16), 2341–2348.

Nitta, T., 1987: Convective activities in the tropical western pacific and their impact on the Northern-Hemisphere summer circulation. *J. Meteorol. Soc. Japan*, **65**, 373–390.

Pan, L.-L., and T. Li, 2008: Interactions between the tropical ISO and midlatitude low-frequency flow. *Climate Dyn.*, **31**(4), 375–388.

Ray, P., C. D. Zhang, J. Dudhia, et al., 2009: A numerical case study on the initiation of the Madden-Julian oscillation. *J. Atmos. Sci.*, **66**(2), 310–331.

Saha, S., and Coauthors, 2006: The NCEP climate forecast system. *J. Climate*, **19**, 3483–3517.

Salby, M. L., R. Garcia, and H. H. Hendon, 1994: Planetary-scale circulations in the presence of climatological and wave-induced heating. *J. Atmos. Sci.*, **51**, 2344–2367.

Seo, K.-H., and K.-Y. Kim, 2003: Propagation and initiation mechanism of the Madden-Julian oscillation. *J. Geo. Res.*, **108**, NO. D13, 4384, doi: 10.1029/2002JD002876.

Shinoda, T., and H. H. Hendon, 1998: Mixed layer modeling of intraseasonal variability in the tropical western Pacific and Indian oceans. *J. Climate*, **11**(10), 2668–2685.

Shukla, J., T. N. Palmer, R. Hagedorn, et al., 2010: Toward a new generation of world climate research and computing facilities. *Bull. Amer. Meteor. Soc.*, **91**(10), 1407–1412.

Slingo, J. M., K. R. Sperber, J. S. Boyle, et al., 1996: Intraseasonal oscillation in 15 atmospheric general circulation models: Results from an AMIP diagnostic subproject. *Climate Dyn.*, **12**(5), 325–357.

——, D. P. Rowell, K. R. Sperber, et al., 1999: On the predictability of the interannual behaviour of the Madden-Julian oscillation and its relationship with El Niño. *Quart. J. Roy. Meteor. Soc.*, **125**, 583–609.

Sobel, A. H., and E. D. Maloney, 2000: Effect of ENSO and the MJO on western North Pacific tropical cyclones. *Geophys. Res. Lett.*, **27**(12), 1739–1742.

——, and ——, 2013: Moisture modes and the eastward propagation of the MJO. *J. Atmos. Sci.*, **70**(1), 187–192.

Sperber, K. R., 2003: Propagation and the vertical structure of the Madden-Julian oscillation. *Mon. Wea. Rev.*, **131**(12), 3018–3037.

——, and T. N. Palmer, 1996: Interannual tropical rainfall variability in general circulation model simulations associated with the atmospheric model intercomparison project. *J. Climate*, **9**, 2727–2750.

——, J. M. Slingo, P. M. Inness, et al., 1997: On the maintenance and initiation of the intraseasonal oscillation in the NCEP/NCAR reanalysis and in the GLA and UKMO AMIP simulations. *Climate Dyn.*, **13**(11), 769–795.

Stephens, G. L., P. J. Webster, R. H. Johnson, et al., 2004: Observational evidence for the mutual regulation of the tropical hydrological cycle and tropical SST. *J. Climate*, **17**(11), 2213–2224.

Straub, K. H., and G. N. Kiladis, 2003: Interactions between the boreal summer intraseasonal oscillation and higher-frequency tropical wave activity. *Mon. Wea. Rev.*, **131**(5), 945–960.

Takaya, K., and H. Nakamura, 2001: A formulation of a phase-independent wave-activity flux for stationary and migratory quasigeostrophic eddies on a zonally varying basic flow. *J. Atmos. Sci.*, **58**(6), 608–627.

Takayabu, Y. N., and T. Nitta, 1993: 3–5 day period disturbances coupled with convection over the tropical Pacific Ocean. *J. Meteor. Soc. Japan*, **71**, 221–246.

Vecchi, G. A., and D. E. Harrison, 2002: Monsoon breaks and subseasonal sea surface temperature variability in the Bay of Bengal. *J. Climate*, **15**(12), 1485–1493.

Waliser, 2006: Intraseasonal Variability. *Asian Monsoon*, B. Wang, Ed., Springer, Heidelberg, Germ, 787 pp.

——, K.-M. Lau, and J.-H. Kim, 1999: The influence of coupled sea surface temperatures on the Madden-Julian oscillation: A model perturbation experiment. *J. Atmos. Sci.*, **56**, 333–358.

——, R. Murtugudde, and L. E. Lucas, 2003: Indo-Pacific Ocean response to atmospheric intraseasonal variability. Part I: Austral summer and the Madden-Julian oscillation. *J. Geophys. Res-Oceans*, **108**(C5), 3160, doi: 10.1029/2002JC001620.

Wang, B., 1988: Dynamics of tropical low-frequency waves: An analysis of the moist Kelvin wave. *J. Atmos. Sci.*, **45**(14), 2051–2065.

——, and H. Rui, 1990a: Synoptic climatology of transient tropical intraseasonal convection anomalies, 1975–1985. *Meteor. Atmos. Phys.*, **44**(1–4), 43–61.

——, and ——, 1990b: Dynamics of the coupled moist Kelvin-Rossby wave on an equatorial β-plane. *J. Atmos. Sci*, **47**(4), 397–413.

——, and T. Li, 1993: A simple tropical atmospheric model of relevance to short-term climate variation. *J. Atmos. Sci.*, **50**, 260–284.

——, and T. Li, 1994: Convective interaction with boundary-layer dynamics in the development of a tropical intraseasonal system. *J. Atmos. Sci.*, **51**(11), 1386–1400.

——, and X. Xie, 1998: Coupled modes of the warm pool climate system. Part I: The role of air-sea interaction in maintaining Madden-Julian oscillation. *J. Climate*, **11**(8), 2116–2135.

——, J.-Y. Lee, J. Shukla, et al., 2009: Advance and prospectus of seasonal prediction: Assessment of the APCC/CliPAS 14-model ensemble retrospective seasonal prediction (1980–2004). *Climate Dyn.*, **33**(1), 93–117.

——, and F. Liu, 2011: A model for scale interaction in the Madden-Julian oscillation. *J. Atmos. Sci.*, **68**(11), 2524–2536.

Wang, L., T. Li, T. Zhou, et al., 2013: Origin of the intraseasonal variability over the North Pacific in boreal summer. *J. Climate*, **26**(4), 1211–1229.

Weickmann, K. M., 1983: Intraseasonal circulation and outgoing longwave radiation modes during Northern Hemisphere winter. *Mon. Wea. Rev.*, **111**(9), 1838–1858.

——, G. R Lussky, and J. E. Kutzbach, 1985: Intraseasonal (30–60 day) fluctuations of outgoing longwave radiation and the 250-mb streamfunction during northern winter. *Mon. Wea. Rev.*, **113**(6), 941–961.

Wheeler, M., and H. H. Hendon, 2004: An all-season real-time multivariate MJO index: Development of an index for monitoring and prediction. *Mon. Wea. Rev.*, **132**, 1917–1932.

Wu, M. L. C., S. D. Schubert, M. J. Suarez, et al., 2005: Seasonality and meridional propagation of the MJO. *J. Climate*, **19**(10), 1901–1921.

Yanai, M., S. Esbensen, and J.-H. Chu, 1973: Determination of bulk properties of tropical cloud clusters from large-scale heat and moisture budgets. *J. Atmos. Sci.*, **30**, 611–627.

Yang Hui and Li Chongyin, 2003: The relation between atmospheric intraseasonal oscillation and summer severe flood and drought in the Changjiang-Huaihe River basin. *Adv. Atmos. Sci.*, **20**(4), 540–553.

Yang, J, B. Wang, B. Wang, et al., 2010: Biweekly and 21–30-day variations of the subtropical summer monsoon rainfall over the lower reach of the Yangtze River basin. *J. Climate*, **23**(5), 1146–1160.

Yasunari, T., 1979: Cloudiness fluctuation associated with the Northern Hemisphere summer monsoon. *J. Meteor. Soc. Japan*, **57**, 227–242.

——, 1980: A quasi-stationary appearance of 30–40 day period in the cloudiness fluctuation during summer monsoon over India. *J. Meteor. Soc. Japan*, **58**, 225–229.

Zhang, C., 2005: Madden-Julian oscillation. *Rev. Geophys.*, **43**, RG2003, doi: 10.1029/2004RG000158.

Zhao, C.-B., T. Li, and T. Zhou, 2013: Precursor signals and processes associated with MJO initiation over the tropical Indian Ocean. *J. Climate*, **26**, 291–307.

Zheng, Y., D. E. Waliser, W. Stern, et al., 2004: The role of coupled sea surface temperatures in the simulation of the tropical intraseasonal oscillation. *J. Climate*, **17**, 4109–4134.

Zhou C., and T. Li, 2010: Upscale feedback of tropical synoptic variability to intraseasonal oscillations through the nonlinear rectification of the surface latent heat flux. *J. Climate*, **23**(21), 5738–5754.

Zhu, C. W., T. Nakazawa, J. Li, et al., 2003: The 30–60 day intraseasonal oscillation over the western North Pacific Ocean and its impacts on summer flooding in China during 1998. *Geophys. Res. Lett.*, **30**(18), 1952, doi: 10.1029/2003GL017817.

Zhu, W., T. Li, X. Fu, et al., 2010: Influence of the maritime continent on the boreal smmer intraseasonal oscillation. *J. Meteor. Soc. Japan*, **88**, 395–407.